Investigation of the Performance of a Method to Reduce Pile Driving Generated Underwater Noise

Dejie Zhou

A thesis
submitted in partial fulfillment of the
requirements for the degree of

Master of Science in Engineering (Mechanical Engineering)

University of Washington

2009

Program Authorized to Offer Degree:
Mechanical Engineering

TABLE OF CONTENTS

1 Introduction

Many human activities such as underwater pile driving generate loud underwater sounds that can in some instances cause biological damage to marine life. The specific effects of pile driving on marine life depends on a wide range of factors including the type of pile, type of hammer, species, animal size, and environmental setting [2] . Most studies on underwater noise due to construction have focused on biological effects on marine life, and little effort has been focused on actually solving the noise problem. Therefore, there is an urgent need for new methods of reducing noise generation during construction, especially for underwater pile driving.

There are at least two possible causes of the radiated acoustic energy from the pile as shown in Figure 1.1. The first cause is the dispersive bending waves that are excited by the hammer blow. The second cause is the expansion of the pile due to the compression from the hammer. There are a number of potential approaches to reduce the radiated acoustic energy from the pile, such as adjusting pile stroke parameters and prolonging the impulse contact time. [1] However, we are particularly interested in two approaches. The first one is to reduce the ability of the vibrating pile from generating sound by using bubbles in close proximity of the surface of the driven pile. The second approach, which

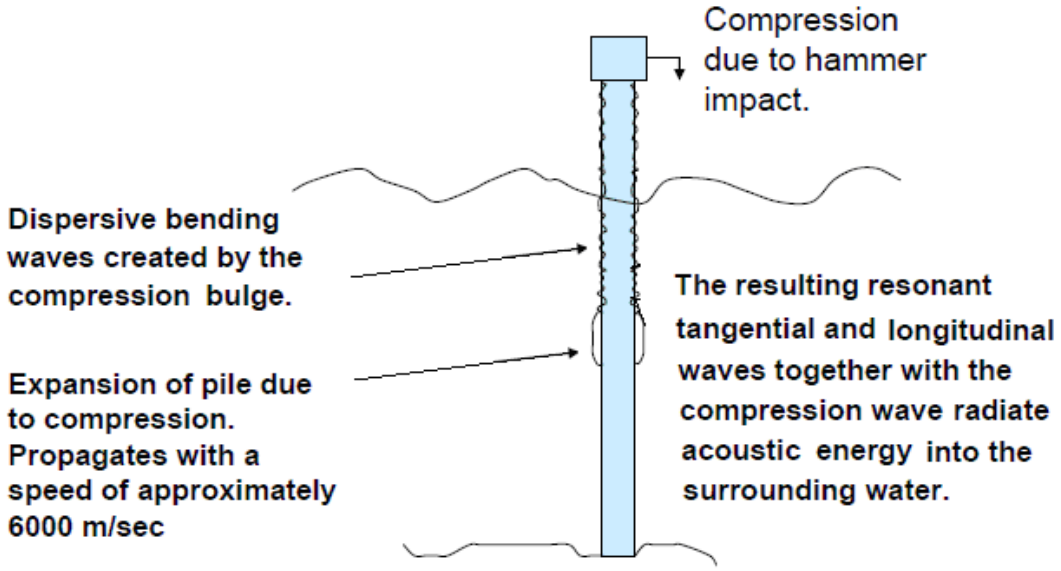

Figure 1.1 Vibration during pile driving

is addressed in this study, is to provide noise attenuation by implementing a double-walled tube surrounding the driven pile. In order to gain better understanding of underwater noise associated with the vibrating pile and the performance of the candidate noise attenuation measures, the Washington State Department of Transportation (WSDOT) conducted a number of underwater pile driving tests just northeast of the Mukilteo Ferry Terminal in Seattle, Washington, in November 2006 and in February of 2007. During the tests, a hydrophone was positioned at mid-water level and located at a distance of 10 meters [4] from the driven pile as shown in Figure 1.2. A total of 8 test piles were driven. In this study, we analyzed the test results from two of these piles. The first pile, named T2, is a pile that was driven into the sediment without any noise attenuation treatment. The second pile, R4, was surrounded by a

protective shield to decrease the generated noise. Specifically, pile T2 is a 80 ft long steel pipe that has 36 inch outer diameter (OD) with 1 inch wall thickness.

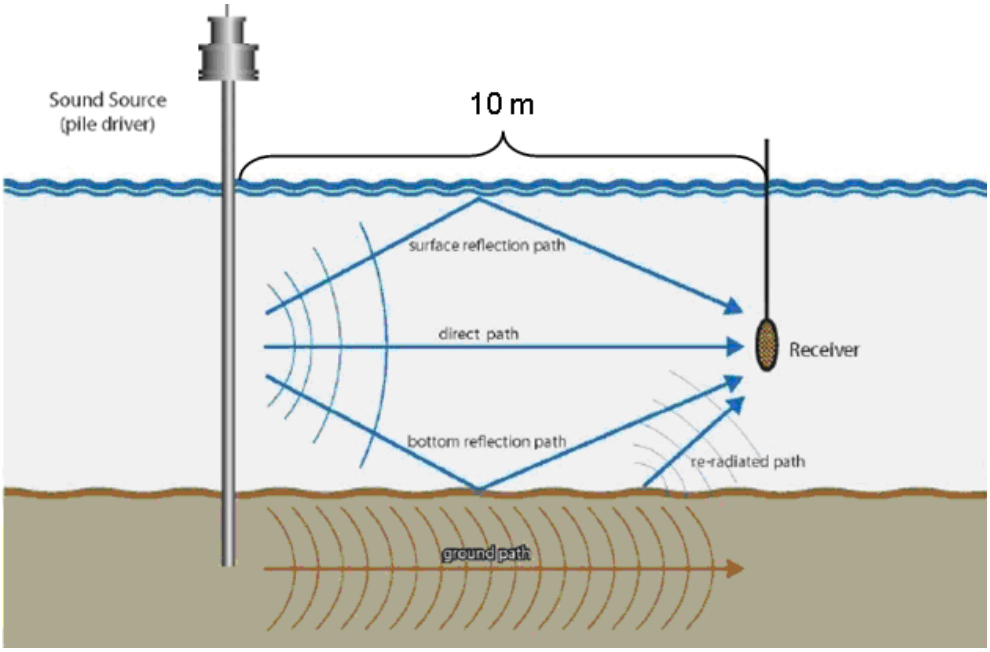

Figure 1.2 The setup of the pile driving test

Pile T2 was driven in water depth of 27 feet in relatively soft sediments in November 2006. The test data of unmitigated pile T2 is investigated in this study. Pile R4 is a 89 ft long steel pipe which also has 36 inch OD, 1 inch thick. It was driven in water depth of 24 feet in February 2007. This pile was surrounded by a double walled Temporary Noise Attenuation Pile (TNAP). In this study, the TNAP specifically refers to TNAP-1 which was the hollow double walled steel pile casing placed around pile R4. The TNAP consisted of an inner pipe and an outer pipe with a 2-inch air gap between the two pipes. The inner pipe had a 48 inch OD, and a wall thickness of 3/8 inch and the pipe

was 48 ft long, whereas the outer pipe was 48 ft long steel pipe with 54 inch OD and 1/2 inch wall thickness. The schematics of pile T2, and the TNAP

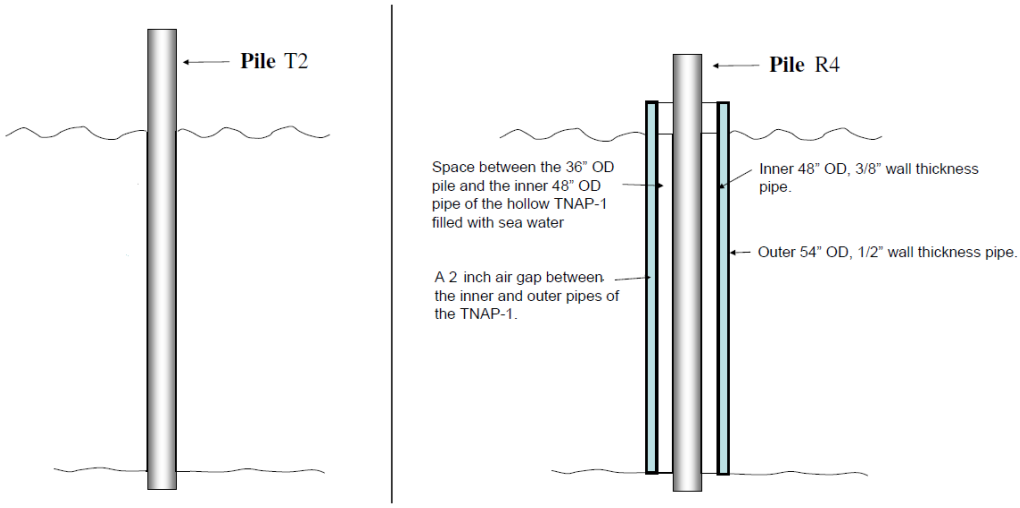

Figure 1.3 The schematic of pile T2 and the TNAP protected pile R4

protected pile R4 are shown in Figure 1.3 and their dimensions are listed in Table 1.1. The TNAP and raw pile tests were conducted four months apart, and their direct comparison is complicated by this fact. Thus, although their comparison is carried out in this work, strictly speaking this thesis represents a study of two separated systems.

Table 1.1 Dimensions of pile T2, pile R4, TNAP

Dimension Parameters (in meters)	Pile T2 (Raw Pile)	Pile R4 (Raw Pile)	TNAP Inner Pipe	TNAP Outer Pipe
Total Length L	24.384	27.128	14.631	14.631
Mean Radius R	0.4445	0.4445	0.6093	0.6855
Thickness h	0.0254	0.0254	0.009525	0.0127
Wetted Length L_{wet}	8.23	7.315	7.315	7.315

This study is organized as follows. Chapter 2 presents the investigation on whether the noise level of both pile T2 and the TNAP protected pile R4 comply with the latest noise compliance standards, which were set by the regulatory bodies in June 2008 [3]. Chapter 3 and 4 are devoted to investigate which range of structural modes of a pipe are more likely to be significantly excited when it is subjected to excitation from hammer strikes. In Chapter 4,

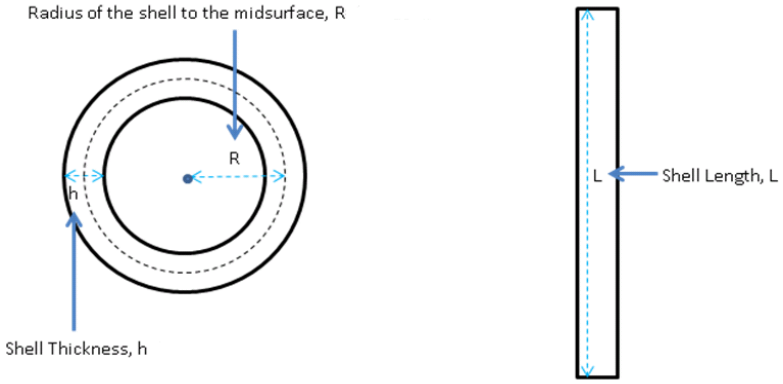

Figure 1.4 Dimensional parameters of a pipe (not to scale)

we also identify the range of the excited modes which can be effectively attenuated by the candidate damping material. Moreover, the variations of the mean energy spectral density curve of both piles are discussed in Chapter 5, and the time-frequency analysis of both pile T2 and pile R4 are performed in Chapter 6. In addition to the study of the transmission loss across the TNAP, areas of future improvement are identified in Chapter 7. Finally, the possible modal density and vibration patterns of pile T2 and the outer pipe of the TNAP at their corresponding observed peak frequencies are investigated with ANSYS in Chapter 8, and a conclusion is given in Chapter 9.

2 Measurements of Underwater Sound

There is no clear consensus which aspects of the pile noise signal are relevant when considering how underwater sound may impact marine life. In order to provide some understanding of the possible metrics for describing sound characteristics relevant to potential disturbance and injury, a number of metrics are currently used by regulatory bodies [5], such as cumulative sound exposure level (cumulative SEL), peak pressure level (L_{peak}), and root mean square pressure level (RMS). The definitions of these three metrics and their corresponding interim criteria with regard to injuring marine life from underwater pile driving are introduced in this chapter. Subsequently, we discuss the test data of pile T2 and the TNAP protected pile R4 with respect to these interim criteria. Because underwater pile driving affects marine life in different locations is still an on going research, policies and guidelines are in an iterative and self-correcting process, so they will continue to evolve as new data become available.

Moreover, it is important to standardize the point at which the acoustic signals are measured for a determination of when the criteria are exceeded. Based on current procedures, this distance is 10 meters from the source [8]. All interim criteria on noise thresholds at 10 m range from the marine construction

noise source are shown in Table 2.1 below. In this chapter, we discuss the test results of pile T2 and the TNAP protected pile R4 with respect to all threshold values in the red circle of Table 2.1.

Table 2.1 Marine mammal, fish, and marbled murrelet injury and disturbance threshold limits for marine construction activities [6]

Functional Hearing Group	Airborne Noise Thresholds	Underwater Noise Thresholds	
	In air Sound Pressure Level (RMS)	Impact Pile Driving Disturbance Threshold	Injury Threshold
Cetaceans	NA	160 dB RMS	180 dB RMS
Pinnipeds	Disturbance: 90 dB RMS (un-weighted) for harbor seals, and 100 dB RMS (un-weighted) for sea lions and all other pinnipeds (re: 20 µPa²sec)	160 dB RMS	190 dB RMS
Fish ≥ 2 grams	NA	Behavior effects threshold 150 dB RMS	187 dB Cumulative SEL
Fish < 2 grams	NA		183 dB Cumulative SEL
Fish all sizes	NA		206 dB Peak
Foraging marbled murrelets	Injury: 92 dBA	150dB RMS	180 dB Peak

For pile driving, these are the thresholds that NMFS has determined would result in Level A Harassment (injury) and Level B Harassment (disturbance) to marine mammals .

2.1 Sound Exposure Level (SEL) of a Single Acoustic Event and Cumulative SEL of Successive Acoustic Events

For pulsed sounds such as underwater pile driving noise, they are not only measured in term of peak pressure, but also in term of energy because the duration of the pulsed sound may be a contributor to potential biological damage. SEL measures the acoustic energy of the pulse in transient, it is the total energy produced from a single noise event. SEL defined in Equation 2.1 frequently being used for human noise exposures, and has recently been suggested as a possible metric to quantify impacts to fish [7].

$$SEL = 10\log_{10}\{\int_{t_1}^{t_2}\frac{[P(t)]^2}{P_{ref}^2}dt\} \quad \textbf{(2.1)}$$

where P(t) is the pressure of the acoustic event. P_{ref} =1μPa is the reference pressure for underwater acoustic events. t_1 and t_2 are the starting time and ending time of the acoustic event, respectively. The selection points of t_1 and t_2 are illustrated in Figure 2.1 below. The unit of SEL is dB re 1μPa²*Sec.

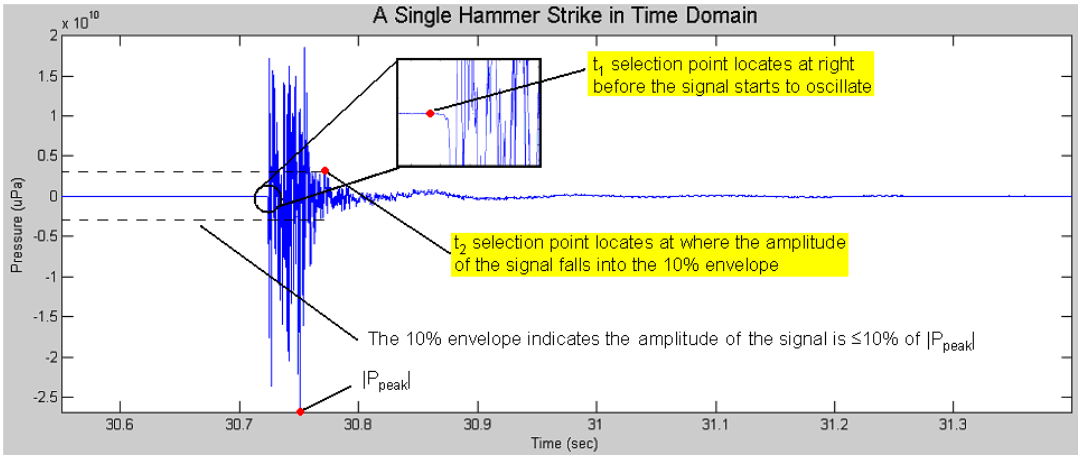

Figure 2.1 Time interval selection points

The SEL values of all strikes on pile T2 and the TNAP protected pile R4 are shown in Figure 2.2. If is believed that a cumulative effect leads to greater risk of injury, the SEL of a single acoustic event may or may not be an appropriate metric for measuring repetitive sounds. The cumulative SEL criteria are used by the regulatory bodies [3]. Specifically, the interim criteria threshold limit on cumulative SEL for fish ≥2 g is 187 dB; for fish <2 g, the threshold is 183 dB (Table 2.1). Assuming no recovery between strikes and all strikes have the same SEL value, the cumulative SEL can be computed with Equation 2.2, and the

definition of the single strike SEL is shown in Equation 2.1.

$$\text{Cumulative SEL} = 10 \log_{10} (\#\text{ of strikes}) + \text{Single Strike SEL} \quad \textbf{(2.2)}$$

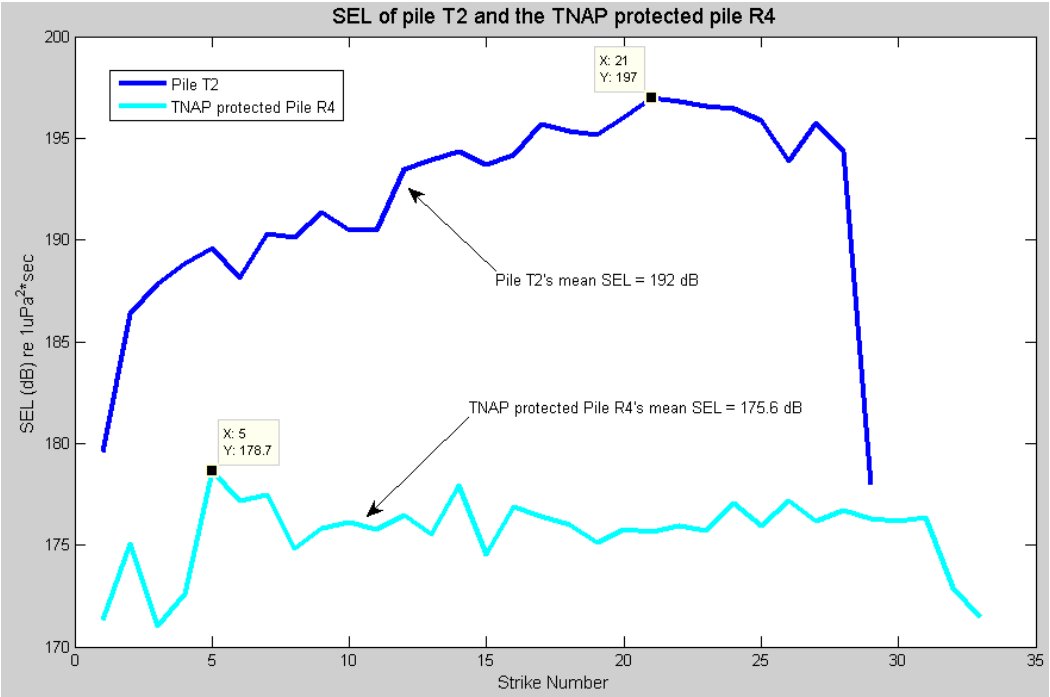

Figure 2.2 SEL of pile T2 and pile R4

Since the SEL values of the individual strikes on pile T2 and pile R4 vary, we calculate the cumulative SEL with both maximum single strike SEL and mean single strike SEL from Figure 2.2 and compare the computed results, which are listed in Table 2.2, to the 187 dB_{SEL} and 183 dB_{SEL} interim criteria threshold limits. According to the results in Table 2.2, the cumulative SEL of pile T2 breaches both 187 dB_{SEL} and 183 dB_{SEL} limits more than 24 dB regardless which single strike SEL is used. In contrast, the cumulative SEL of the TNAP protected pile R4 also exceeds both 187 dB_{SEL} and 183 dB_{SEL} limits by at least 4 dB. In other words, neither the noise level of pile T2 nor the noise level of the

TNAP protected pile R4 complies with the cumulative SEL criteria.

Table 2.2 Cumulative SEL of pile T2 and pile R4

Pile Name	# of Strikes	Max Single Strike SEL	Mean Single Strike SEL	Cumulative SEL based on Max Single Strike SEL	Cumulative SEL based on Mean Single Strike SEL	Cumulative SEL Injury Threshold Limits
Pile T2	29	197 dB	192 dB	211.6 dB	206.6 dB	187 dB (Fish≥2g) 183 dB (Fish<2g)
TNAP protected Pile R4	33	178.7 dB	175.6 dB	194 dB	191 dB	187 dB (Fish≥2g) 183 dB (Fish<2g)

2.2 Peak Pressure Level (L_{Peak})

Peak pressure level (L_{peak}) is the maximum excursion of pressure within a pulse. L_{peak} is defined as the following:

$$L_{peak} = 20\log_{10}\left(\frac{|P_{peak}|}{P_{ref}}\right) \quad \textbf{(2.3)}$$

where P_{peak} is the instantaneous maximum of the absolute value of the sound pressure observed. P_{peak} can either be the highest positive pressure or the lowest negative pressure. P_{ref} =1μPa is the reference pressure for underwater acoustic events. The unit of L_{peak} is dB re 1μPa. The L_{peak} values of all strikes on pile T2 and the TNAP protected pile R4 with respect to the interim threshold limit are shown in Figure 2.3 below. The regulatory bodies did not specify the size of the fish regard to the L_{peak} limit. However, they suggest fish should not be exposed to pulsed sound that has L_{peak} exceeding 206 dB_{peak} [6]. According to Figure 2.3,

nearly 52% of the strikes of the unprotected pile T2 breach the 206 dB_{peak} limit for fish, and the observed absolute maximum L_{peak} value of pile T2 exceeds the 206 dB_{peak} limit by more than 7 dB. On the other hand, the L_{peak} values of the

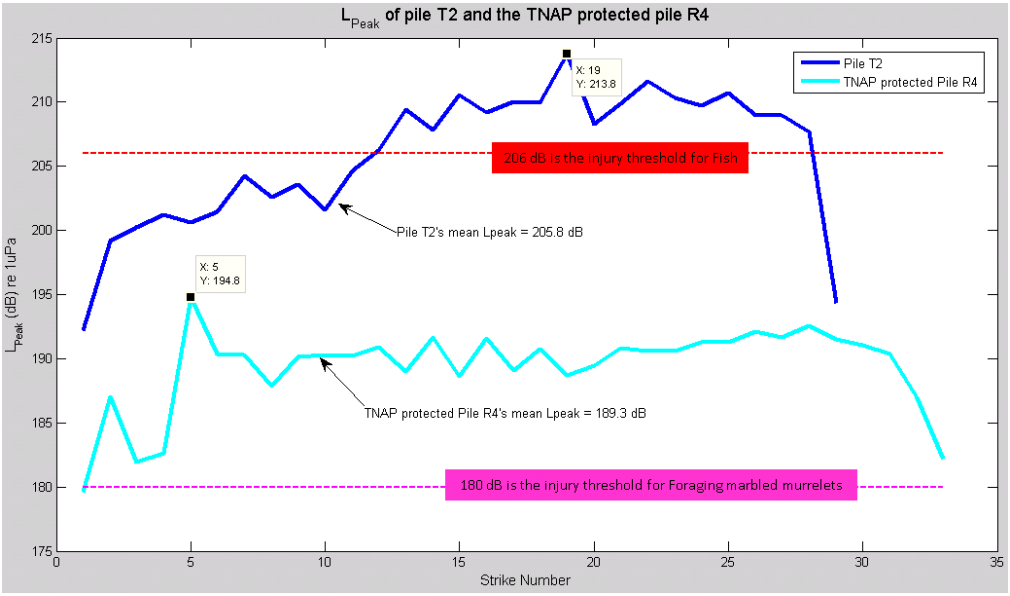

Figure 2.3 L_{peak} of pile T2 and pile R4 with respect to the threshold limits

TNAP protected pile R4 are all below the 206 dB_{peak} limit for fish, but most of the strikes still exceed the 180 dB injury threshold for foraging marbled murrelets by 9 dB as Figure 2.3 indicates.

2.3 Root Mean Square Pressure Level (RMS)

RMS has been used by National Marine Fisheries Service (NMFS) in criteria for judging impacts to marine mammals from underwater impulse-type sounds [4]. Short transient sounds are often described in terms of peak pressure, while longer transients and continuous sounds are more typically expressed in

terms of RMS. Specifically, the RMS is the square root of the energy divided by the impulse duration as shown in Equation 2.4 and 2.5. It is the mean square pressure level of the pulse. The unit of RMS is dB re 1μPa.

$$P_{rms} = \sqrt{\frac{1}{t_2 - t_1}\int_{t_1}^{t_2}[P(t)]^2\,dt} \tag{2.4}$$

$$RMS = 10\log_{10}\left(\frac{P_{rms}^2}{P_{ref}^2}\right) \tag{2.5}$$

where $P_{ref} = 1\mu Pa$ is the reference pressure for underwater acoustic events. The RMS values of all strikes on pile T2 and pile R4 with respect to the threshold limits, which are used by NMFS, are shown in Figure 2.4 below. According to Figure 2.4, most of the strikes on pile T2 exceed both 190 dB_{RMS} and 180 dB_{RMS}

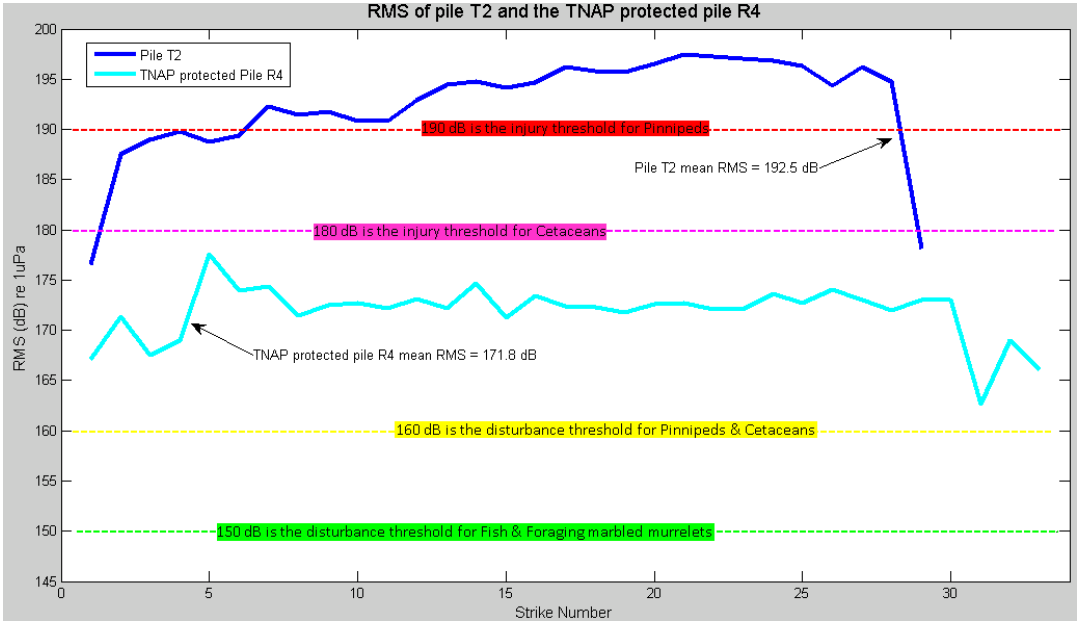

Figure 2.4 RMS of pile T2 and pile R4 with respect to the threshold limits

injury threshold for Pinnipeds and Cetaceans. On the other hand, the RMS values of all strikes on the TNAP protected pile R4 are below the injury

thresholds for both Cetaceans and Pinnipeds, but these values are still above the 160 dB_{RMS} disturbance threshold for Pinnipeds and Cetaceans, and the 150 dB_{RMS} disturbance threshold for Fish and Foraging marbled murrelets as Figure 2.4 indicates.

In summery, the peak pressure level limits the absolute maximum acoustic pressure of a single hammer blow, whereas the cumulative SEL imposes acoustic energy allowance restrictions on successive hammer strikes within a finite time window. The results suggest the cumulative SEL values of pile T2 and the TNAP protected pile R4 exceed the interim criteria of injuring fish by at least 24 dB and 4 dB, respectively. Whereas the L_{peak} values of 52% of the strikes on pile T2 breach the 206 dB_{peak} threshold limit of injuring fish, while the L_{peak} values of the TNAP protected pile R4 are still high enough to not satisfy the criterion of injuring Foraging marbled murrelets. Finally, all RMS values of the TNAP protected pile R4 are well above the disturbance limits for Cetaceans, Pinnipeds, Fish and Foraging marbled murrelets.

3 The Structural Pile Model

It is important to identify the possible vibration modes of an excited pipe at its most energetic natural frequencies since they may be sources of noise

during underwater pile driving. This chapter introduces a structural pipe model for the natural frequencies of a pipe associated with its structural modes. These modes are expected to play some role, at least in part, in determining peaks in the frequency spectra of the radiated sound from an impact excited pipe. The investigation is divided up into two parts. The first part is devoted to the identification of the shell modes, and the second part is dedicated to the identification of the breathing and beam modes. The model in this work was originally derived by Sharma [11], and was validated with experimental data by Blevins [10]. The following six assumptions are made:

1. The pipe has constant wall thickness.

2. Thin shell theory defined as pipe wall thickness being less than 10% of the pipe radius.

3. The pipe is composed of a linear, elastic, homogeneous and isotropic material.

4. The pipe is not pre-loaded.

5. Rotary inertia and shear deformation are neglected.

6. The deformations of the pipe wall are small in comparison with the thickness of the pipe wall. No nonlinear effects are therefore included.

3.1 Identifying the shell modes

The higher cylindrical modes of a pipe involve circumferential deformation that can be described only by shell theory [10]. Approximate formulas have been developed to describe these modes. The accuracy of these approximate formulas generally increases with the circumferential mode number, *i*, and the value of $\frac{L}{jR}$, where L is the shell length, *j* is the axial mode number and R is the mean radius of the shell. A general expression for the deformations of a freely vibrating cylindrical shell is:

$$\begin{aligned} u &= A\phi_j'(\frac{x}{L})\cos(i\theta)\cos(\omega t) \\ v &= B\phi_j'(\frac{x}{L})\sin(i\theta)\cos(\omega t) \\ w &= C\phi_j'(\frac{x}{L})\cos(i\theta)\cos(\omega t) \end{aligned} \qquad \textbf{(3.1)}$$

where ϕ_j' is the axial mode shape. A, B, C are constants which describe the amplitude of the axial (u), tangential (v), and radial (w) deformations of the shell midsurface. $\omega=2\pi f$ is the circular natural frequency of vibration; f is natural frequency of the cylindrical shell defined in Equation 3.4. *i* is the number of

circumferential wave in the mode shape and *j* is the number of longitudinal half-waves in the mode shape. A few examples of how *i* or *j* values correspond to a particular vibration mode shape of a cylindrical shell are illustrated in Figure 3.1.

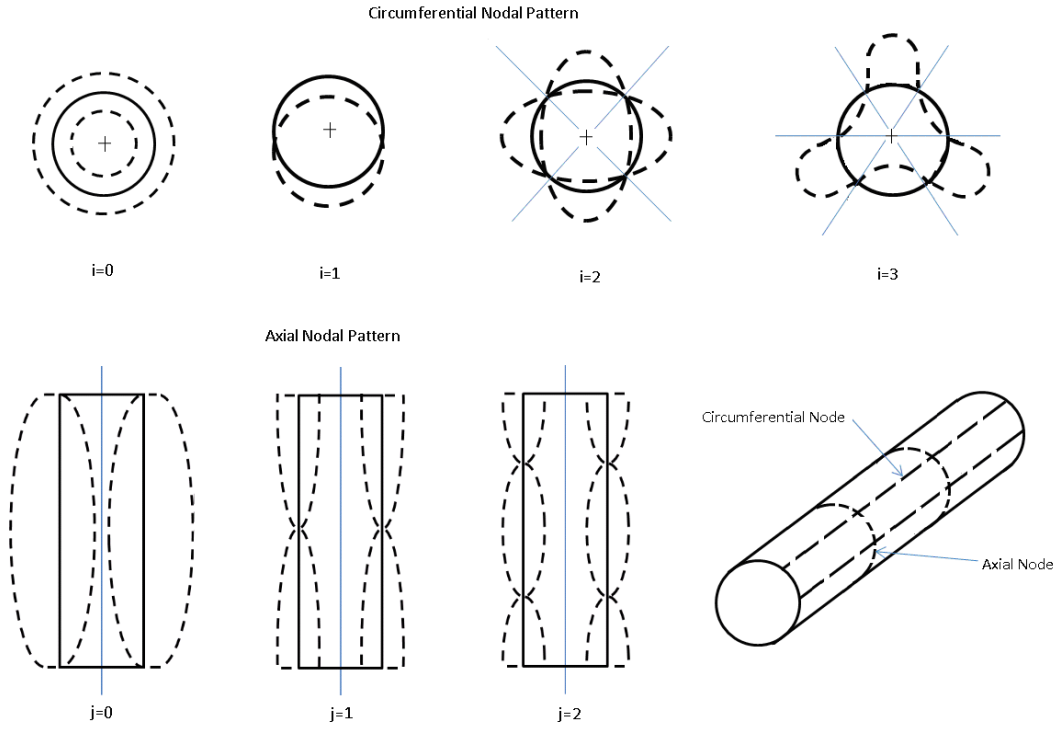

Figure 3.1 Circumferential and axial nodal patterns of a cylindrical shell

In conjunction with the Flügge shell theory and the Rayleigh-Ritz technique, the following characteristic equation is produced for the natural frequencies and mode shapes of a cylindrical shell [10]:

$$\begin{bmatrix} a_{11}-\alpha_2\lambda_{ij}^2 & a_{12} & a_{13} \\ a_{12} & a_{22}-\lambda_{ij}^2 & a_{13} \\ a_{13} & a_{23} & a_{33}-\lambda_{ij}^2 \end{bmatrix} \begin{bmatrix} A \\ B \\ C \end{bmatrix} = 0 \qquad \textbf{(3.2)}$$

By setting the determinant of the characteristic matrix to zero for non-trivial solutions results in the following characteristic polynomial:

$$\alpha_2\lambda_{ij}^6 - \lambda_{ij}^4(a_{11} + \alpha_2 a_{22} + \alpha_2 a_{33}) - \lambda_{ij}^2(a_{12}^2 + a_{13}^2 + \alpha_2 a_{23}^2 - \alpha_2 a_{22}a_{33} - a_{11}a_{33} - a_{11}a_{22})$$

$$+ a_{12}^2 a_{33} + a_{23}^2 a_{11} + a_{13}^2 a_{22} + a_{11}a_{22}a_{33} - 2a_{12}a_{23}a_{13} = 0 \quad \textbf{(3.3)}$$

The dimensionless frequency parameter λ_{ij} can be obtained by solving the above 6th-order polynomial numerically, then the natural frequencies of the shell becomes:

$$f_{ij} = \frac{\lambda_{ij}}{2\pi R}\sqrt{\frac{E}{\rho(1-\upsilon^2)}} \quad \textbf{(3.4)}$$

where E is the modulus of elasticity, ρ is the density of the shell material, υ is the Poisson's ratio. Sharma [11] has developed a second approximate expression for the natural frequency parameter λ_{ij} without solving the 6th-order polynomial numerically, and this approximation equation is listed in Equation 3.5 below.

$$\lambda_{ij} = \sqrt{\frac{(a_{11}a_{22}a_{33} + 2a_{12}a_{13}a_{23} - a_{11}a_{23}^2 - a_{22}a_{13}^2 - a_{33}a_{12}^2)i^4}{(a_{11}a_{22} - a_{12}^2)(\beta_j^2\alpha_2 + i^4 + i^2)}} \quad \textbf{(3.5)}$$

where

$$a_{11} = \beta_j^2 + \frac{1}{2}(1+k)(1-\upsilon)i^2\alpha_2 \quad \textbf{(3.6)}$$

$$a_{12} = -\upsilon i\beta_j\alpha_1 - \frac{1}{2}(1-\upsilon)i\beta_j\alpha_2 \quad \textbf{(3.7)}$$

$$a_{13} = -\upsilon i\beta_j\alpha_1 + k\beta_j[-\beta_j^2 + \frac{1}{2}(1-\upsilon)i^2\alpha_2] \quad \textbf{(3.8)}$$

$$a_{22} = i^2 + \frac{1}{2}(1+3k)(1-\upsilon)\beta_j^2\alpha_2 \quad \textbf{(3.9)}$$

$$a_{23} = i + ki\beta_j^2[\upsilon\alpha_1 + \frac{3}{2}(1-\upsilon)\alpha_2] \quad \textbf{(3.10)}$$

$$a_{33} = 1 + k[\beta_j^4 + (i^2-1)^2 + 2\upsilon i^2\beta_j^2\alpha_1 + 2(1-\upsilon)i^2\beta_j^2\alpha_2] \quad \textbf{(3.11)}$$

$$\beta_j = \frac{\lambda_j R}{L} \quad \textbf{(3.12)}$$

$$k = \frac{h^2}{12R^2} \quad \textbf{(3.13)}$$

R is the mean radius of the shell, h is the shell wall thickness. λ_j is the dimensionless beam frequency parameter given in Table 3.1.

Table 3.1 λ_j vs. j

j	0	1	2	3	4	>4
λ_j	4.73004074	7.85320462	10.9956078	14.1371655	17.2787597	(2j+1)π/2

α_1 and α_2 are integrals of the mode shape, and they are defined as the following:

$$\alpha_1 = -\frac{1}{L}\int_0^L \phi_j''(x)\phi_j(x)dx \quad \textbf{(3.14)}$$

$$\alpha_2 = \frac{1}{L}\int_0^L [\phi_j(x)]^2 dx \quad \textbf{(3.15)}$$

Since the sand cannot prevent the bottom of the pipe from expanding radially, free-free boundary condition is used to estimate the natural frequencies of the pipe. With free-free boundary condition,

$$\alpha_1 = \frac{\sigma_j}{\lambda_j}(\sigma_j \lambda_j - 2) \quad \textbf{(3.16)}$$

$$\alpha_2 = \frac{\sigma_j}{\lambda_j}(\sigma_j \lambda_j + 6) \quad \textbf{(3.17)}$$

where $\sigma_j = \frac{\cosh(\lambda_j) - \cos(\lambda_j)}{\sinh(\lambda_j) - \sin(\lambda_j)}$ **(3.18)**

These equations yield accurate results when circumferential number i≥2 and $\frac{L}{jR} > 8$.

3.2 Identifying the breathing mode and the beam modes

As previously mentioned, higher order modes *i*≥2 of cylindrical shells involving circumferential deformation can be described only by shell theory. However, *i*=2 is not always the lowest mode and a lower mode such as the breathing mode *i*=0 can be estimated with Equation 3.19 [12].

$$f = \sqrt{\frac{E}{\rho * R^2}} \quad \textbf{(3.19)}$$

The bending mode *i*=1 of a long shell ($\frac{L}{jR} > 8$), can be analyzed using classical beam theory, and the dimensionless frequency parameter λ_{ij} of *i*=1 bending mode can be expressed as the following:

$$\lambda_{ij} = \frac{\lambda_j^2}{2\pi(L^2)}\sqrt{\frac{E*I}{m}} \quad \textbf{(3.20)}$$

where λ_j is the dimensionless beam frequency parameter given in Table 3.1, L is the total length of the shell, E is the Young's Modulus, m is the mass per unit length of the shell, and I is the area moment of inertia of a cylindrical shell listed in Equation 3.21 below.

$$I = \frac{\pi}{4}[(R+\frac{h}{2})^4 - (R-\frac{h}{2})^4] \quad \textbf{(3.21)}$$

In conjunction with Equation 3.4, the natural frequencies of the bending modes (i=1) can be identified.

In summery, most of the natural frequencies of a pipe can be estimated based on its dimensional parameters L, R, h, and material parameters E, ρ, ν. For shell modes, i≥2, their natural frequencies can be estimated with shell theory approximate formulas (Equation 3.4 and 3.5). For the breathing mode, i=0, its natural frequency can be estimated with Equation 3.19; whereas for the beam modes, i=1, their natural frequencies can be estimated with the beam theory approximate formulas (Equation 3.4, 3.20, and 3.21).

4 Identification of the Structural Modes of a Model Pipe and the Effectiveness of a Damping Treatment

The model in Chapter 3 yielded the natural frequencies of pipes without fluid loading. However, the conditions of underwater pile driving are more complicated since fluid loading needs to be considered. Therefore, in order to better bridge the gap of the idealized and real situations, a simulated pipe-striking experiment was conducted in air to better understand which resonance modes of a pipe are more likely to be excited by hammer strikes. In this chapter, the energy spectral density (ESD) of the model pipe striking experiment is first analyzed to identify the most energetic natural frequencies of the excited model pipe. Subsequently, the model from Chapter 3 is used to identify which vibration mode shapes of the pipe may have been responsible for which natural frequencies. Such mode shape-natural frequency identification process not only enables us to better understand the possible response of the pipe after it is excited, but the process also helps us to gain better insight into which structural modes of a pipe are more likely to be significantly excited during pile driving. Finally, damping material (Kinetics Noise Control Sound Deadener KDD3553), which may be used to fill the air cavity of future TNAPs, is tested to investigate the noise reduction effectiveness of the material.

4.1 Dimensional parameters of the model pipe

First, a given pipe must have $\frac{h}{R} < 0.1$ to be considered as a cylindrical shell, or the model in Chapter 3 cannot be applied [10]. Where h is the shell wall

thickness, and R is the mean radius of the shell. As specified in Table 4.1, all the pipes of interest in this study satisfy the $\frac{h}{R} < 0.1$ condition.

Table 4.1 Dimensional parameters comparison between real system components and the model pipe

Dimension Parameters (in meters)	Pile T2 (Raw Pile)	Pile R4 (Raw Pile)	TNAP-1 Inner Pipe	TNAP-1 Outer Pipe	Model Pipe
h	0.0254	0.0254	0.009525	0.0127	0.0079
R	0.4445	0.4445	0.619126	0.679451	0.1055
L (total length)	24.3843	27.1275	14.6306	14.6306	0.86
h/R	0.057	0.057	0.0154	0.019	0.075

4.2 Investigate the effectiveness of the damping material

Two tests were conducted to gain a better understanding on which structural modes of the model pipe were significantly excited by the hammer strikes, and how effectively and selectively a candidate damping material reduced these excited modes. The first test was to strike the model pipe without any damping material; this data is labeled as "undamped" in Figure 4.1. The data labeled as "damped" came from the second test with damping material

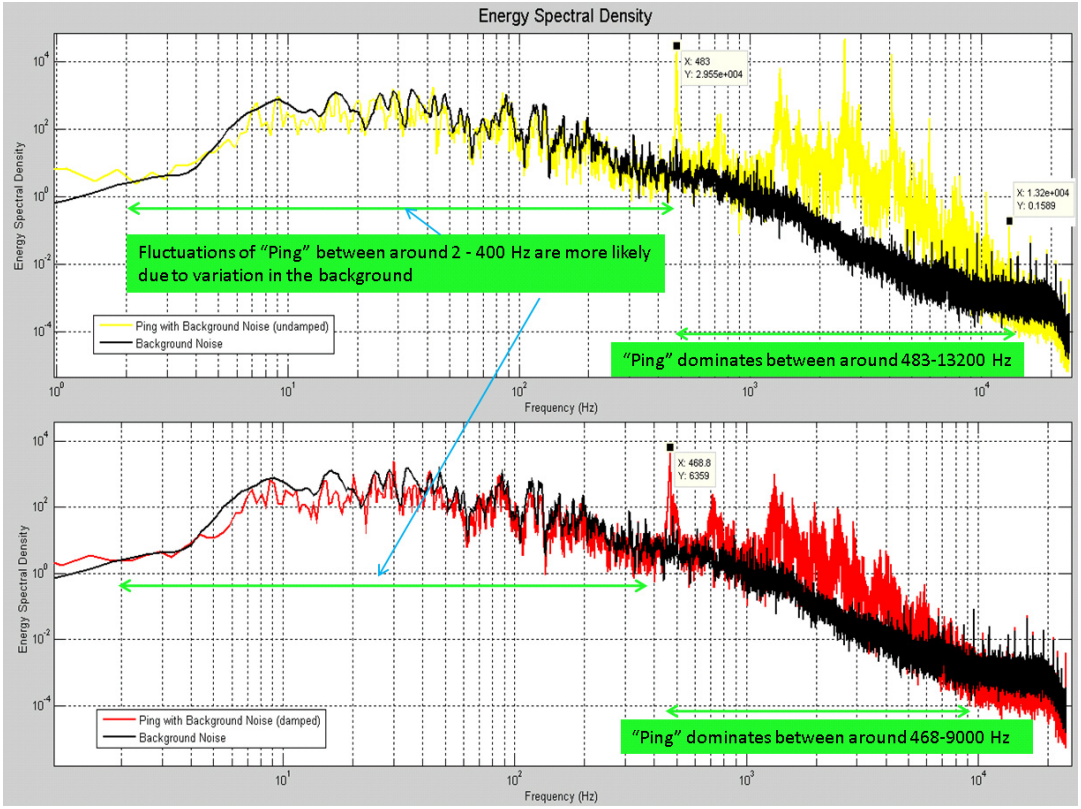

Figure 4.1 ESD of the undamped vs. damped model pipe with respect to background noise

attached to the pipe. In order to identify the excited structural modes of the model pipe and investigate the effectiveness of the damping material, the ESD curves of the experiment data, which are shown in Figure 4.1 and 4.2, are first obtained. As Figure 4.1 indicates, the hammer strikes significantly excited the natural frequencies of the pipe which lie between approximately 460 to 13200 Hz. Whereas most of the fluctuations <460 Hz or >13200 Hz, are most likely due to the activities in the background. By overlapping the undamped and damped signals from Figure 4.1 in Figure 4.2, the effectiveness of the damping material can be easily observed. Figure 4.2 suggests the damping material is

Figure 4.2 ESD of the undamped vs. damped model pipe

more responsive to the excited modes that are ≥ 2500 Hz. Therefore, the primary frequency region of interest is further confined between 460 to 2500 Hz since the excited resonance modes in this region persisted despite the presence of damping material. Hence, further investigation in regards to these modes is necessary and they will be discussed in the next section.

4.3 Identify possible mode shapes of the excited structural modes

The model from the previous chapter is applied to the model pipe, and the subsequent analytical solutions are compared to the experimental values to

identify the vibration mode shapes of the pipe that could have been responsible for the observed peaks between 460 to 2500 Hz. If the % difference between a particular experimental value and its nearest analytical value is <10%, then the mode shape associated with that analytical value is assumed to be responsible for that particular experimental value. The results are shown in Table 4.2.

Table 4.2 List of the experimental and analytical natural frequencies of the model pipe in the primary frequency range of interest

Experimental value of the corresponding natural freq (Hz)	Analytical solution of the corresponding natural freq (Hz)	Modes Circumferential modes (*i*) Axial modes (*j*)
478.6 & 483	487.82	*i*=2, *j*=1
723.6 & 745.6	769.1	*i*=2, *j*=2
1301	1351.48	*i*=3, *j*=1
1348	1351.48 or 1438.45	*i*=3, *j*=1 *i*=3, *j*=2
1440	1475.2 or 1438.45	*i*=2, *j*=3 *i*=3, *j*=2
1627	1660.65	*i*=3, *j*=3
1997	2065.61	*i*=3, *j*=4
2187	2292.32	*i*=2, *j*=4
2565	2586.82	*i*=4, *j*=1
4107	4180.47	*i*=5, *j*=1

The results in Table 4.2 are also presented in Figure 4.3 to better illustrate which vibration mode shape of the pipe is associated with which natural frequency. The upper plot of Figure 4.3 shows the ESD curves of the hammer

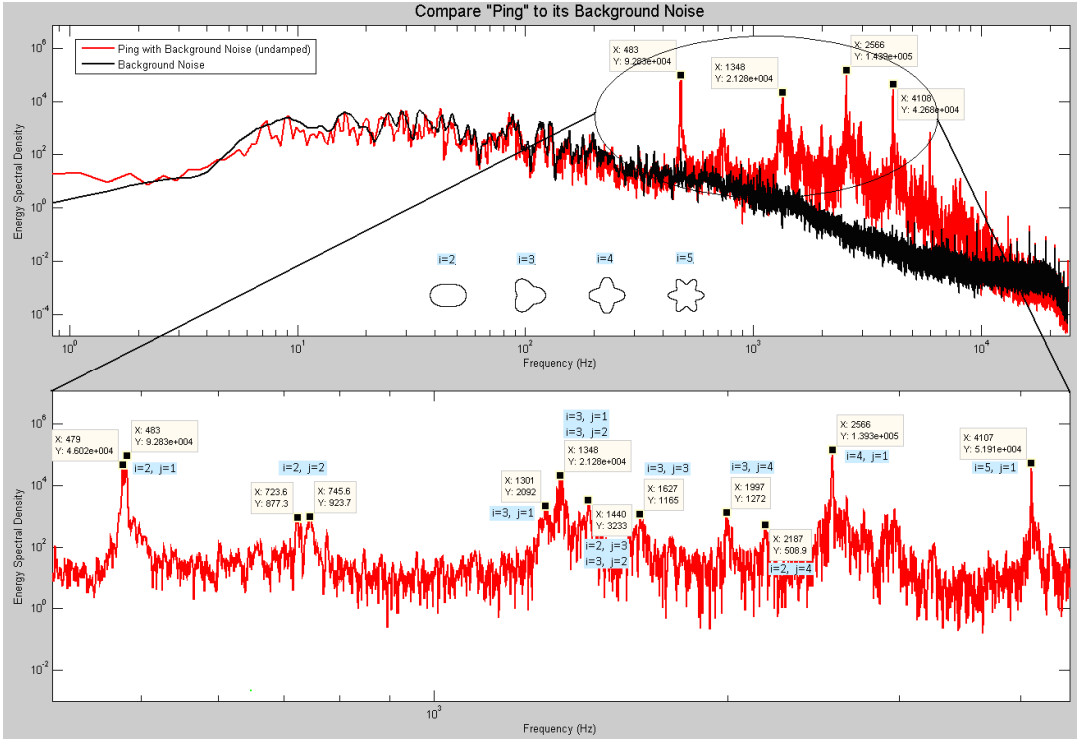

Figure 4.3 The structural modes of the model pipe and their possible vibration mode shapes

strike with respect to its background noise from 0 Hz up to Nyquist frequency; whereas the lower plot is the magnification of the upper plot between 460 to 4150 Hz. All the peaks of the red ESD curve represent the excited structural modes of the model pipe, and the two numbers in each of the blue boxes indicate the circumferential mode number (*i*) and axial mode number (*j*) of its nearest peak. The combination of the circumferential and axial mode numbers represents the possible vibration mode shape of the pipe at the indicated resonance frequency. Moreover, Figure 4.3 suggests the structural modes, that have low circumferential mode number (i=2~4) and low axial mode number (j=1~4), are unaffected by the introduction of the damping treatment.

In summery, the pipe striking experiment indicates the structural modes of the pipe which lie between [480, 13200] Hz were significantly excited by the hammer strikes. Modes which are ≥ 2500 Hz, its energy can effectively be reduced by the candidate damping material. In contrast, for modes that are < 2500 Hz, they were unaffected by the introduction of the damping treatment, and the model suggests these persevere modes involve low circumferential mode (i=2~4) and low axial mode (j=1~4) deformation.

5 Energy Spectral Density Curves from Pile Driving

Since the mean energy spectral density (ESD) curves of pile T2 and the TNAP protected pile R4 will be used extensively in Chapter 7 and Chapter 8, it is important to first find out how well the mean ESD curves represent the rest of the data. Therefore, in this chapter, three investigations are conducted on the mean ESD curves of pile T2 and pile R4. These are: (1) the relative position of the mean ESD curve with respect to the ESD curves of the absolute maximum, absolute minimum, one standard deviation above and below the mean (2) the variations of the peak ESD values, and (3) variations of the peak frequencies. The frequency content is studied up to the Nyquist frequency 12000 Hz.

5.1 Identifying the background noise dominated regions

Before investigating the variations of the mean ESD curve, it is important first to distinguish the hammer strike noise from the background noise. Specifically, the two plots in Figure 5.1 illustrate the relative position of the mean ESD curves of the hammer strikes with respect to the measurement noise floor. The lower plot refers to pile R4, and it suggests that energy in frequencies for pile R4 above 1000 Hz represents a measurement "noise floor". It is possible that the true level is below this level but the hydrophone, designed

for high-level signals, cannot measure it. In contrast, the upper plot (T2) shows results that are well above any measurement noise floor.

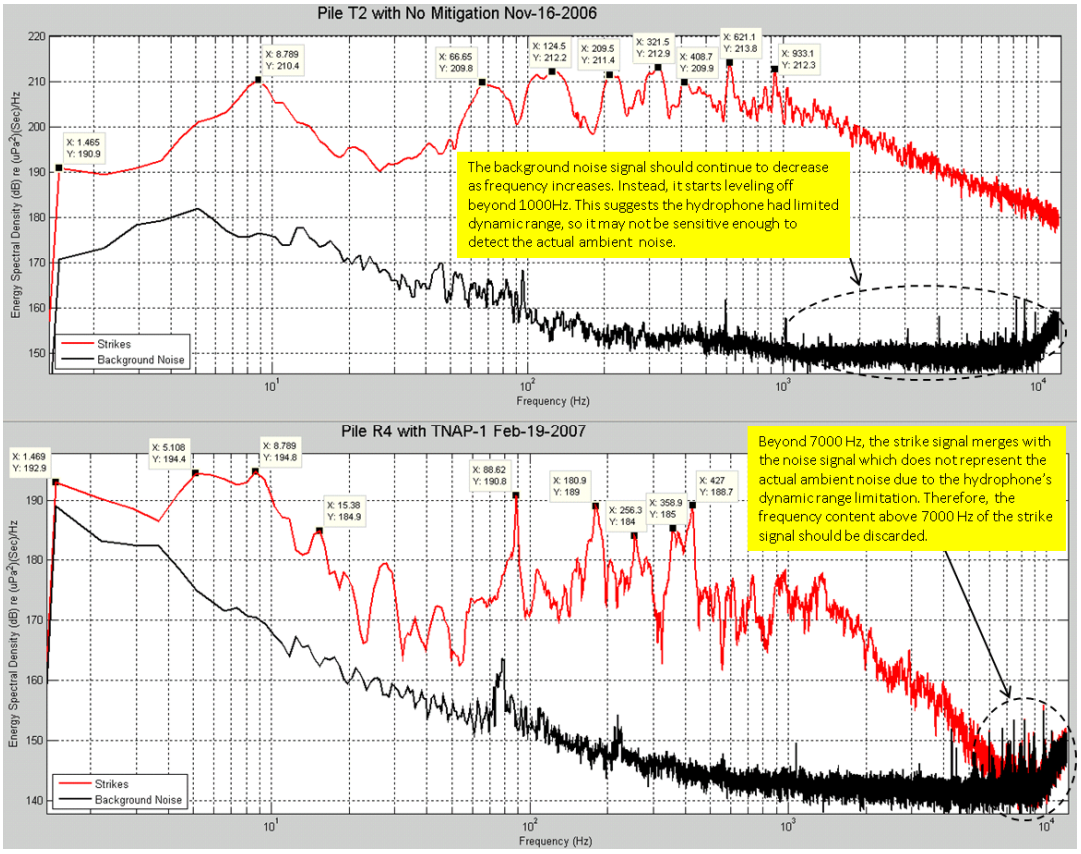

Figure 5.1 Hammer strike signal with respect to background noise signal

5.2 Variations of the ESD curve for pile T2

The upper plot of Figure 5.1 indicates the peak frequencies of pile T2 are below 1000Hz. As the pile being driven deeper into the seabed, some spectral content variations can occur. Therefore, further investigation in regards to these variations is necessary, especially with focus on frequencies that are below 1000 Hz. The ESD curves of the absolute maximum, absolute minimum,

one standard deviation above the mean and one standard deviation below the mean, are plotted along with the mean ESD curve from 0 Hz up to the Nyquist frequency 12000 Hz as shown in Figure 5.2 below to see how far the rest of the data deviate from the mean. According to Figure 5.2, there are eight major peaks located within the frequency region of interest (<1000 Hz), and their corresponding frequencies (X-values) and ESD values (Y-values) are indicated in the textboxes. Because the power of some hammer blows vary greatly from

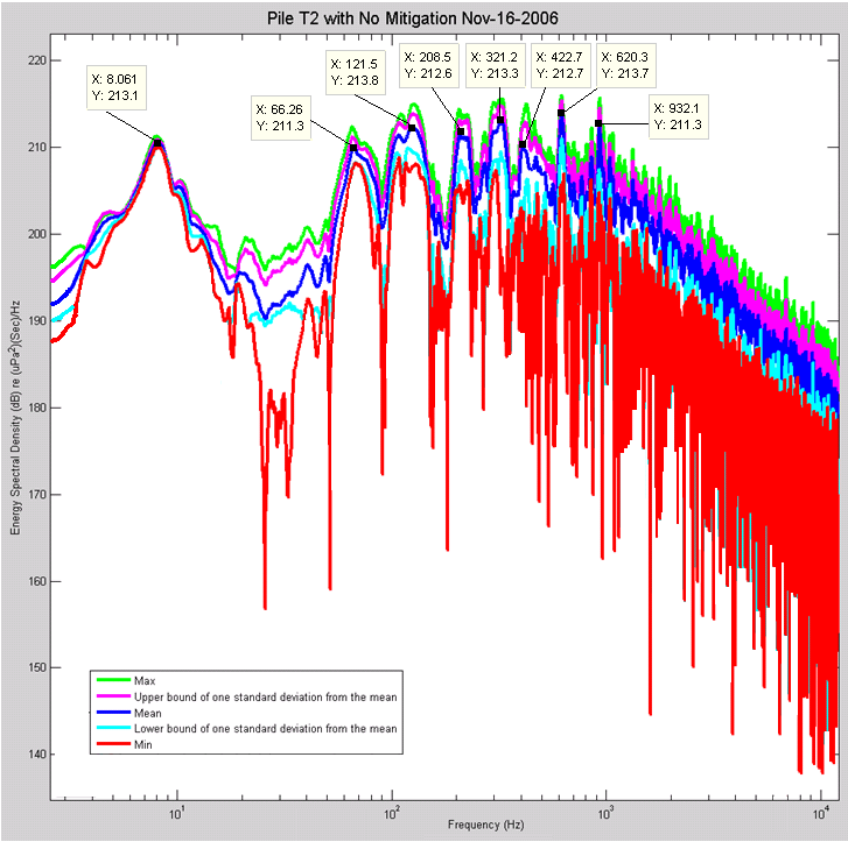

Figure 5.2 Relative position the mean ESD curve for pile T2 with respect to the ESD curves of absolute maximum, absolute minimum, and one standard deviation above and below the mean

the others, some deviations from the mean ESD values are expected. In this case, the most notable deviations come from the absolute minimum ESD

curve. It deviates from the mean ESD curve by at least 15 dB in frequency regions between 20 to 50 Hz. In contrast, the ESD variations in other frequency regions especially at the eight major peaks are mostly contained within 10 dB with respect to the mean. Moreover, the locations of the eight peaks are reasonably aligned which indicates the peak frequencies of all the strikes are mostly consistent.

5.3 Variation of peak ESD values for pile T2

The X and Y values in the eight textboxes of Figure 5.2 indicate the mean peak frequencies and mean peak ESD values of pile T2. In this section, the vertical variations of the eight peak ESD values (Y values in Figure 5.2) through out the course of pile driving are investigated, and they are illustrated in Figure 5.3. A total of 29 strikes were carried out on pile T2, and the 29 dots in each subplot of Figure 5.3 represent the peak ESD values of the 29 strikes. The horizontal axis indicates the strike number, and the vertical axis indicates the peak ESD value, whereas the horizontal black referential line represents the mean peak ESD value. As shown by the black line, the amount of deviation from the mean over the entire pile driving process can be easily observed. In addition, coefficient of variation (standard deviation/mean) is used to quantify how well the mean peak ESD value represents all 29 data points. According to

Figure 5.3, the eight coefficients of variation are much smaller than 1 which suggests the distribution of the 29 data points has low variance. In other words, the mean represents well all 29 data points, and this is true for all eight peaks.

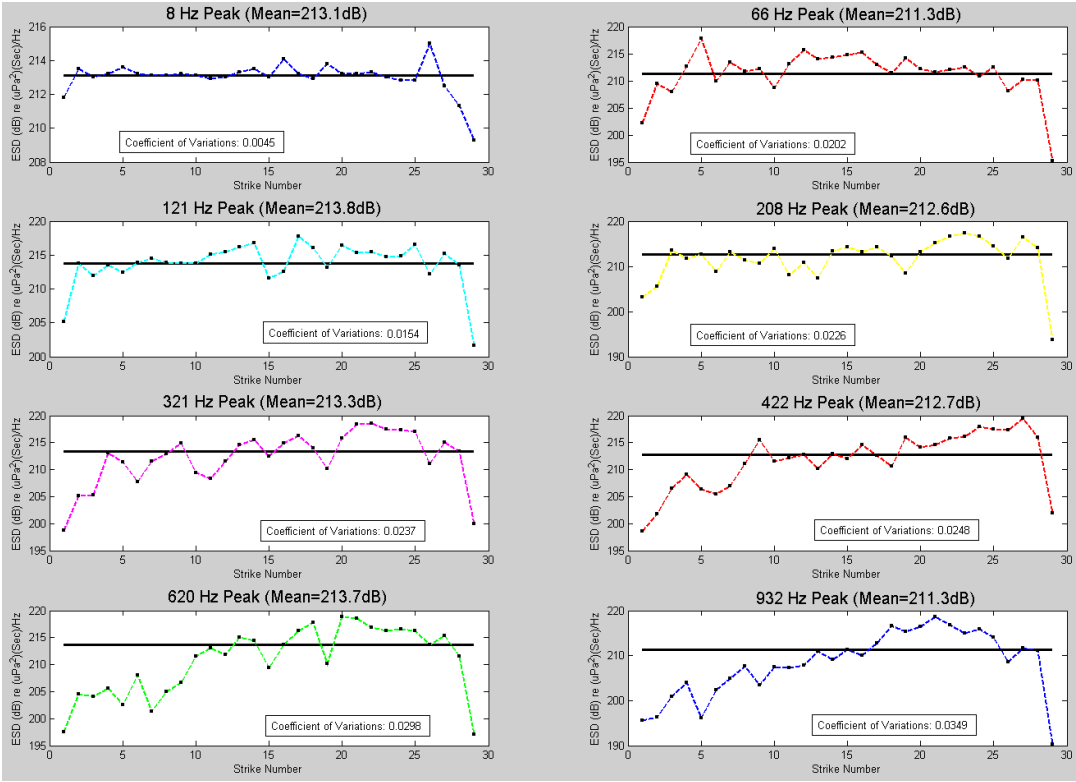

Figure 5.3 Fluctuations of mean peak ESD values for pile T2

5.4 Variation of peak frequencies for pile T2

In this section, the variations of the X values in Figure 5.2 which represent the amount of frequency shifting of the eight peaks are explored, and

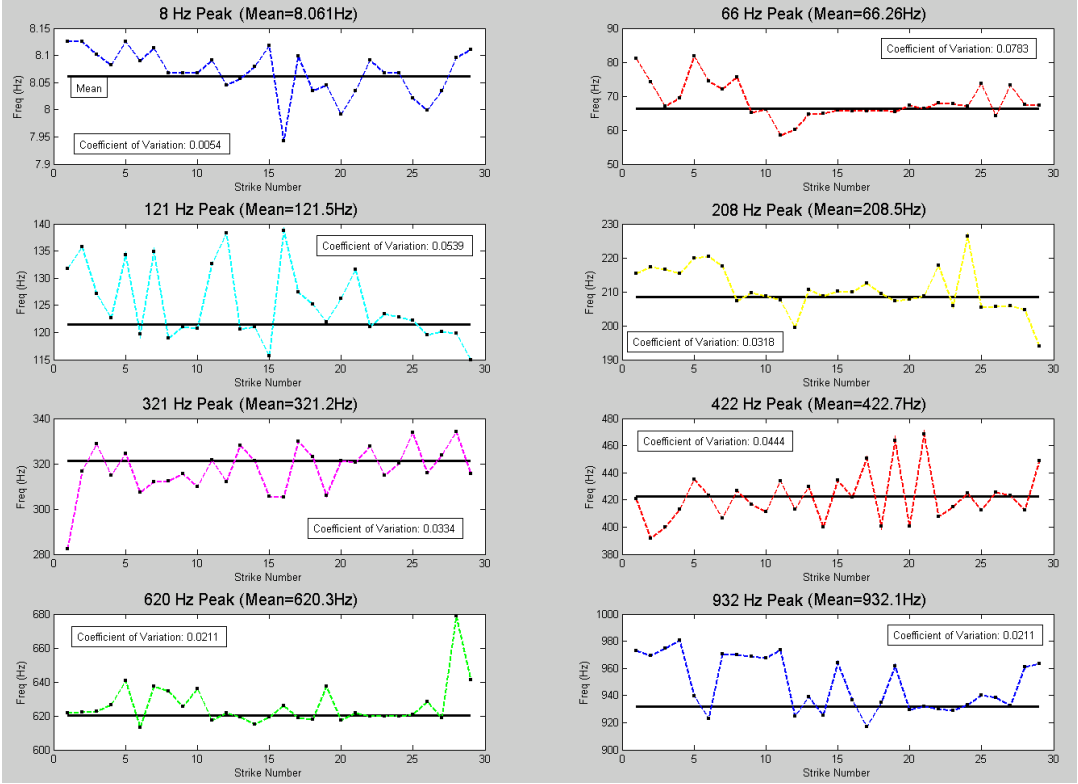

Figure 5.4 Variations of peak frequencies for pile T2

the results are shown in Figure 5.4. The 29 dots in each subplot represent the observed peak frequencies of the 29 strikes. The horizontal axis indicates the strike number, and the vertical axis indicates the observed peak frequency. The horizontal black reference line, which represents the mean observed peak frequency, reveals the amount of frequency shifting from the mean over the entire course of pile driving. The coefficient of variation is used to quantify how well the mean peak frequency represents all the observed values of the 29 strikes. According to Figure 5.4, most of the data points fluctuate closely around the mean reference line, and all eight coefficients of variation are again much smaller than 1 which suggests the degree of scattering of the 29 data

points in each peak is low. Hence, the mean values of the eight peaks will represent their corresponding observed peak frequencies.

5.5 Variations of the ESD curve for pile R4

While the lower plot of Figure 5.1 suggests the primary frequency region of interest of pile R4 locate between 4 to 500 Hz, there are twelve major peaks locate within such region as Figure 5.5 indicates. The vertical variations in other

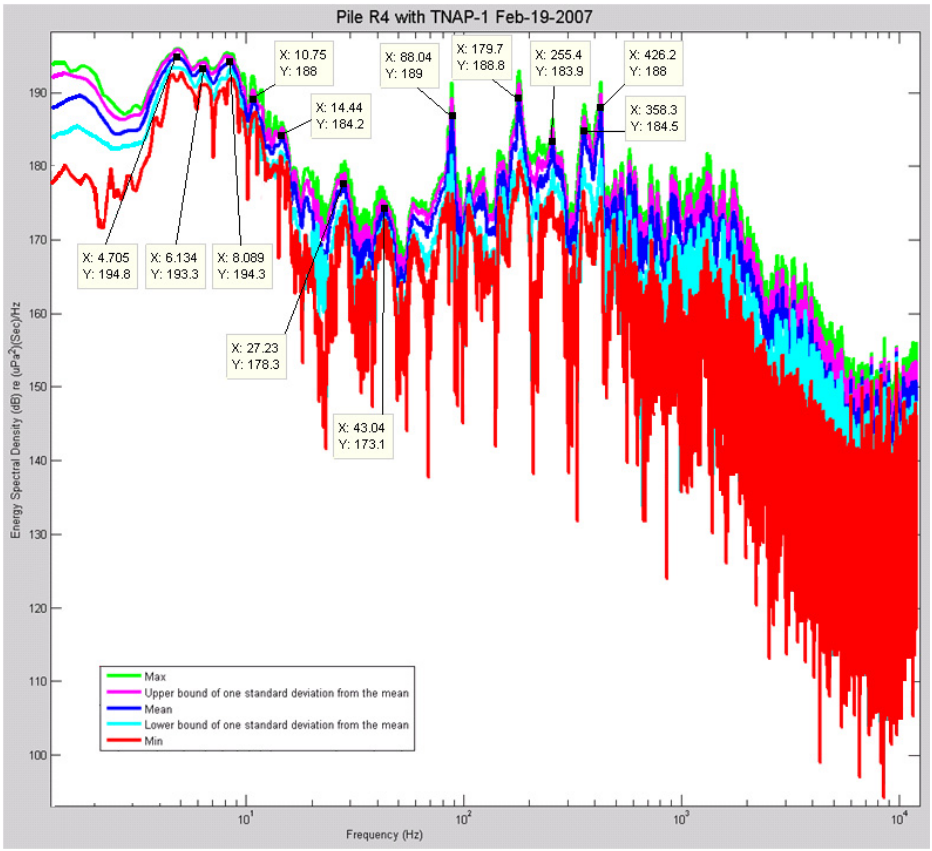

Figure 5.5 Relative position of the mean ESD curve for pile R4 with respect to the ESD curves of absolute maximum, absolute minimum, and one standard deviation above and below the mean

frequency regions especially at the twelve major peaks are mostly contained within 10 dB with respect to the mean, and the horizontal locations of the twelve peaks are also mostly align which indicates the peak frequencies of all strikes are mostly consistent as well.

5.6 Variation of peak ESD values for pile R4

The vertical variation of the twelve peak ESD values (Y values in Figure 5.5) through out the course of pile driving is discussed in this section. Total of 33 strikes were carried out on pile R4 and the 33 dots in each subplot represent

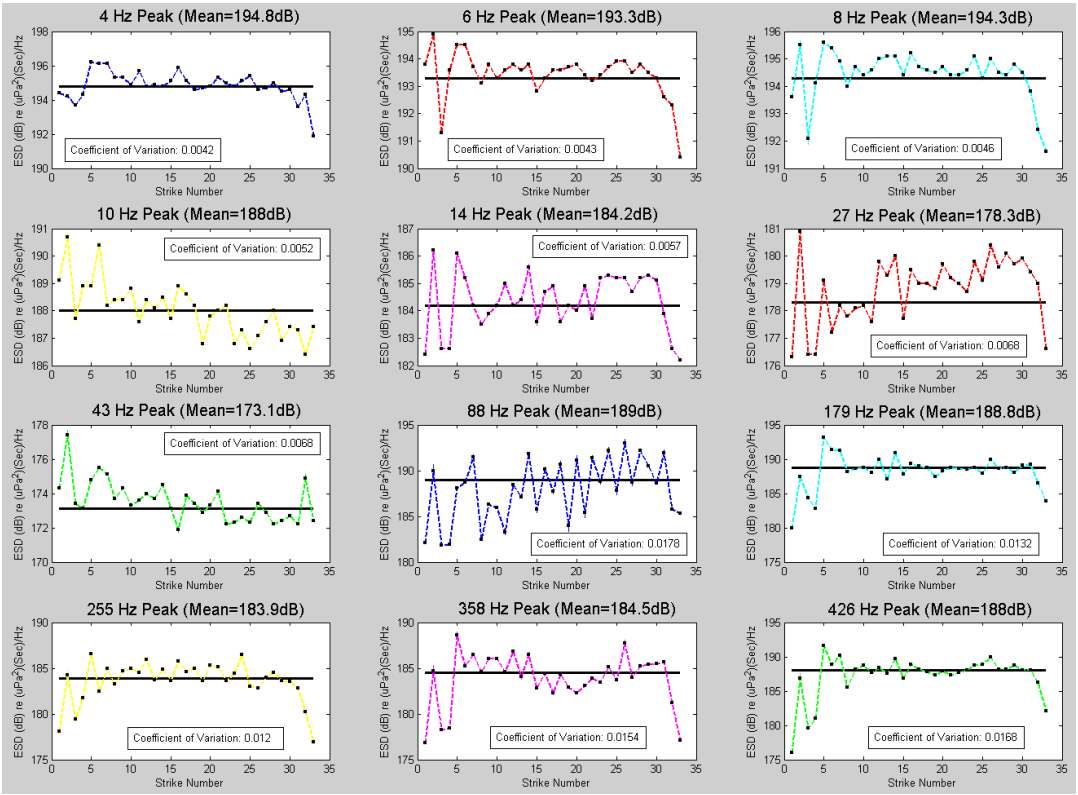

Figure 5.6 Fluctuations of mean peak ESD values for pile R4

the peak ESD values of the 33 strikes. The horizontal axis indicates the strike number, and the vertical axis indicates the peak ESD value. As before, the horizontal black reference line, which represents the mean peak ESD value, illustrates the amount of fluctuation from the mean over the entire pile driving process. According to Figure 5.6, the coefficients of variation of all twelve peaks are much smaller than 1 which suggests the distribution of the 33 data points has low variance.

5.7 Variation of peak frequencies for pile R4

The variation of peak frequencies for pile R4 as a function of strike number is explored in this section. The 33 dots in each subplot of Figure 5.7 represent the observed peak frequencies of the 33 strikes. The horizontal axis indicates the strike number, the vertical axis indicates the observed peak frequency values, and the horizontal referential black line represents the mean observed peak frequency. According to Figure 5.7, most of the data points fluctuate closely around the mean referential line, and all twelve coefficients of variation are considerably less than 1.

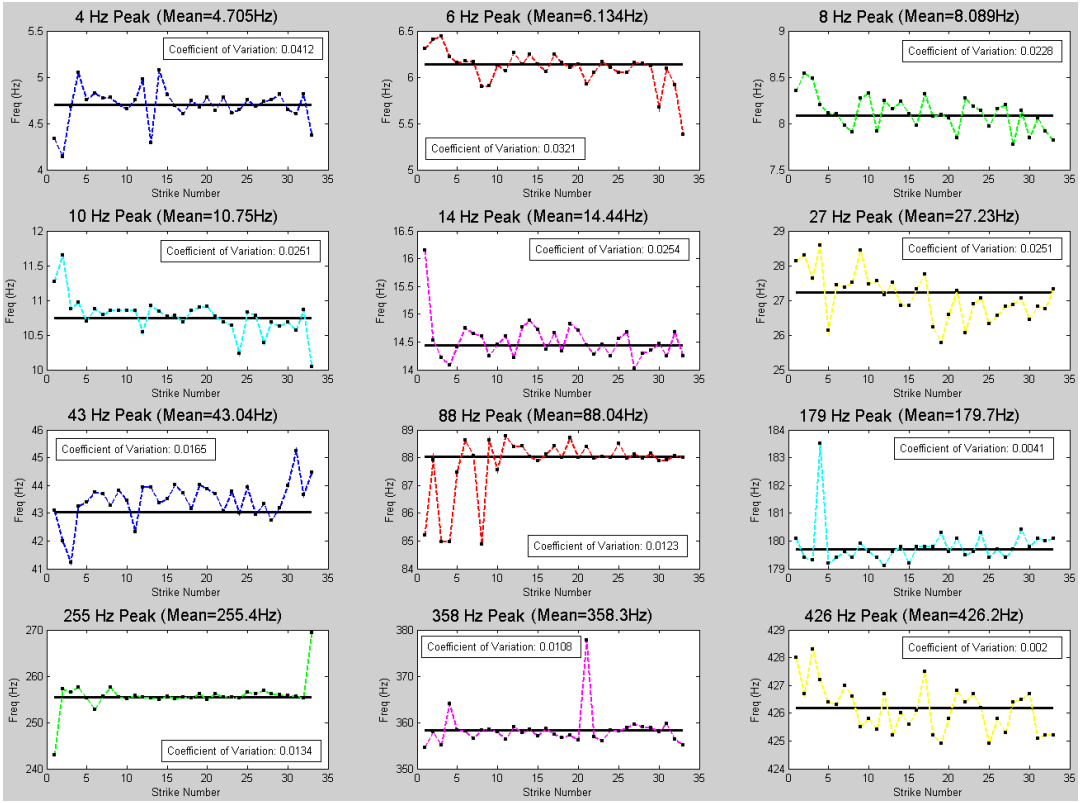

Figure 5.7 Variations of peak frequencies for pile R4

In summery, the mean ESD curves of pile T2 and pile R4 well represent the rest of the data across frequency spectrum from 3 Hz up to 12000 Hz. Since their magnitudes of variation are small, all mean peak ESD values and mean peak frequency values for pile T2 and pile R4 are consistent as a function of strike number.

6 Time-Frequency Analysis

Time-frequency analysis is used to characterize signals with frequency content that vary with time. In this chapter, we use spectrograms to investigate how the spectral density of underwater pile driving events vary with time. We first look at the differences in time-frequency evolution between pile T2 and pile R4. Subsequently we investigate the consistency of the time-frequency content of the two piles through out the whole pile driving process.

6.1 Obtaining the spectrogram

First, the spectrograms in this study are created by using the short-time Fourier transform in MATLAB. The time domain data is initially broken up into segments, and they slightly overlap each other. A Fourier transform is then performed to calculate the magnitude square of the frequency spectrum for each segment. All the spectrograms in this study have the same input parameters which are listed in Table 6.1. The selection of "strike of interest" in

Table 6.1 Parameters for generating the spectrograms of pile T2 and pile R4

MATLAB spectrogram input parameters	Selected signal of interest	Window	Number of data point overlapping (noverlap)	FFT length (nfft)	Sampling frequency (fs)
Actual input	strike of interest	kaiser (150,5) [9]	140	2048	24000

Table 6.1 is illustrated in the first row of Figure 6.1. All selected strike segments, which are used to generate the spectrograms, have equal length.

6.2 Compare the time-frequency content of pile T2 and pile R4

The results in Chapter 5 suggest the spectral content variation of pile T2 and pile R4 as a function of strike number is small. Therefore, only one spectrogram from each pile is selected and compared side by side in this section, to study sound reduction characteristics of the TNAP. This comparison assumes that conditions for the two tests, e.g., hammer type, strike force, and measurement conditions, were the same when in fact these are not known. However, it is of interest to evaluate the two cases from the standpoint of better understanding the physics of noise containment. In Chapter 2, one of the two metrics to quantify underwater pile driving impacts to fish is the sound exposure level SEL (dB re $1\mu Pa^2*sec$) which is directly proportional to the squared pressure of the detected acoustic event. On the other hand, the spectral density (dB re $1\mu Pa^2/Hz$) that is represented by different colors in the spectrogram is also directly proportional to the squared pressure of the detected acoustic event within a specified frequency band. In other words, the intensity of the red color in these spectrograms gives a qualitative indication of the sound exposure level. The color calibration bars of both pile T2 and pile R4 have the

same scale. The left half of Figure 6.1 illustrates the time series and the corresponding spectrogram of the unmitigated pile T2. Whereas the time series and spectrogram of the TNAP protected pile R4 are shown in the right half of

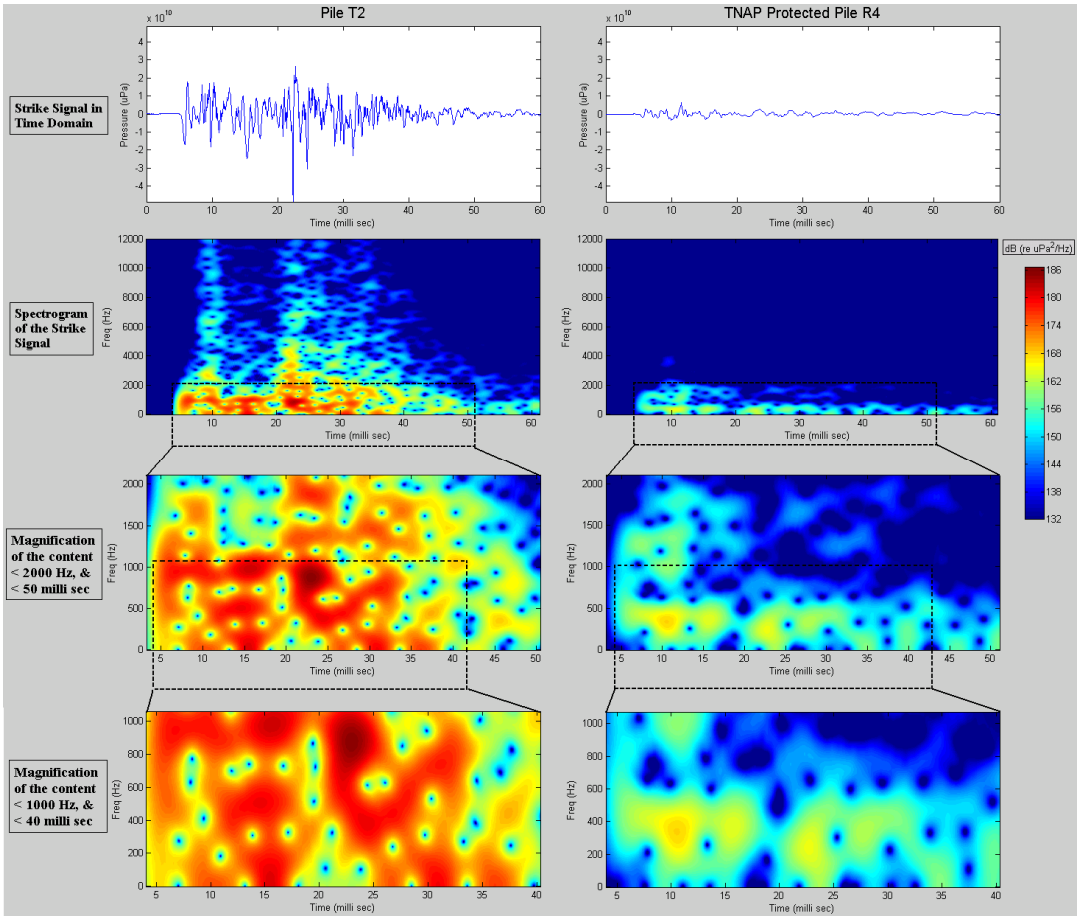

Figure 6.1 Time series and spectrogram comparison between pile T2 and pile R4

Figure 6.1. A comparison of the spectrograms in the second row of Figure 6.1 indicates most of the noise <2000 Hz of the driven pile were clearly mitigated and the noise >2000 Hz mostly vanished. These two observations suggest the TNAP is capable of reducing noise across the frequency spectrum up to the highest frequency observed as determined by Nyquist sampling considerations,

or 12000 Hz, and the device is especially effective for mitigating noise above 2000 Hz. However, it is still noisy below 2000 Hz. As a reminder, the TNAP and raw pile tests were conducted four months apart, and their direct comparison is complicated by this fact. Thus, although their comparison is carried out in this work, strictly speaking this thesis represents a study of two separated systems.

6.3 Investigate the consistency of the time-frequency content

A small amount of spectral content variations along the pile driving process were observed in Chapter 5, as both pile T2 and pile R4 were continuously driven into the seabed. Hence, it is important to further verify the consistency of the spectral content and identify the pile driving noise dominated frequency regions though out the whole pile driving process, so noise attenuation measures can be more effectively implemented. Therefore, the consistency of the time-frequency content with varying strike number is examined. A total of 29 strikes were carried out on pile T2, and three representative strikes were chosen to study how spectral content varies in time-frequency space as the pile being driven further into the ground. The time series and spectrograms of the three representative strikes are shown in Figure 6.2.

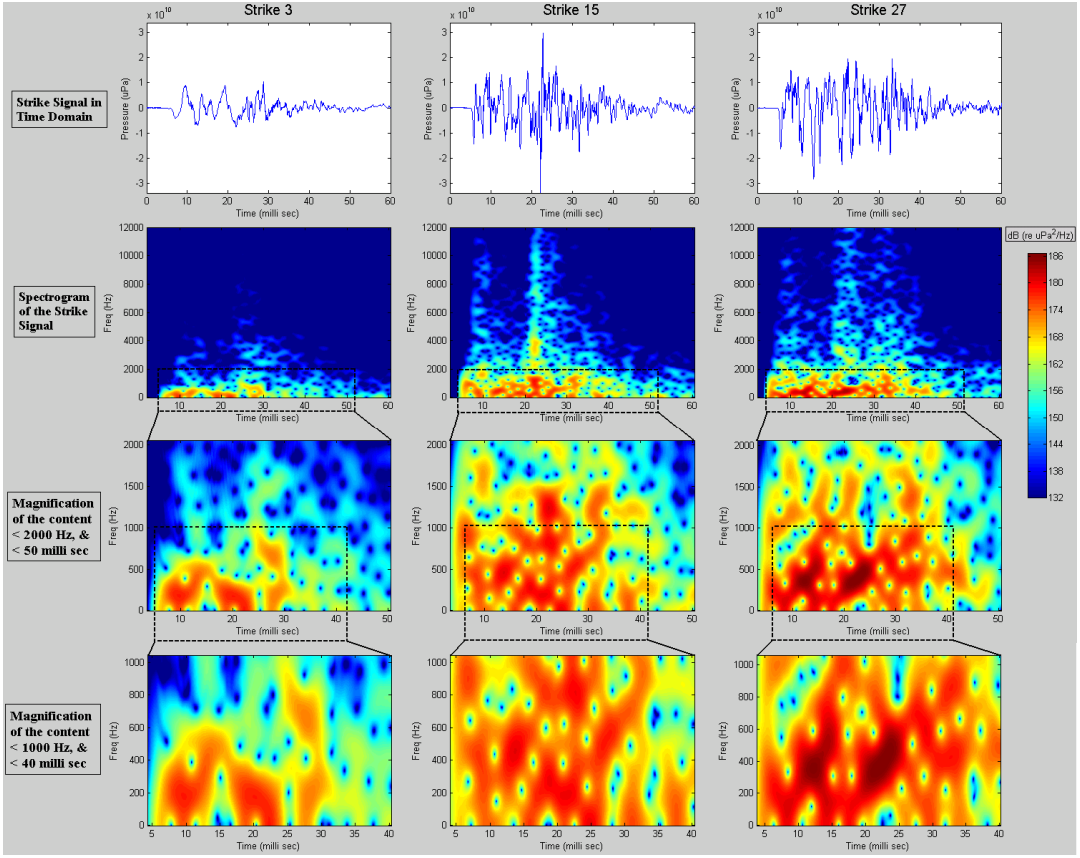

Figure 6.2 Time series and spectrograms of pile T2 as the pile driving process progress

The "structure" of the hot spots (the reddish spots in the spectrograms), which refer to the content whose magnitude exceed 174 dB (re 1μPa²/Hz), varies slightly from strike to strike. However, it is more crucial to focus on where these hot spots appear most frequently though out the entire pile driving process. According to Figure 6.2, the hot spots consistently occur at below 1500 Hz with the most energetic ones locate between 200 to 1000 Hz. Similarly, three representative strikes were chosen to study how spectral content of the TNAP protected pile R4 varies in time-frequency space as the pile being driven

further into the ground. The time series and spectrograms of the three selected strikes are shown in Figure 6.3. A total of 33 strikes were carried out on pile R4.

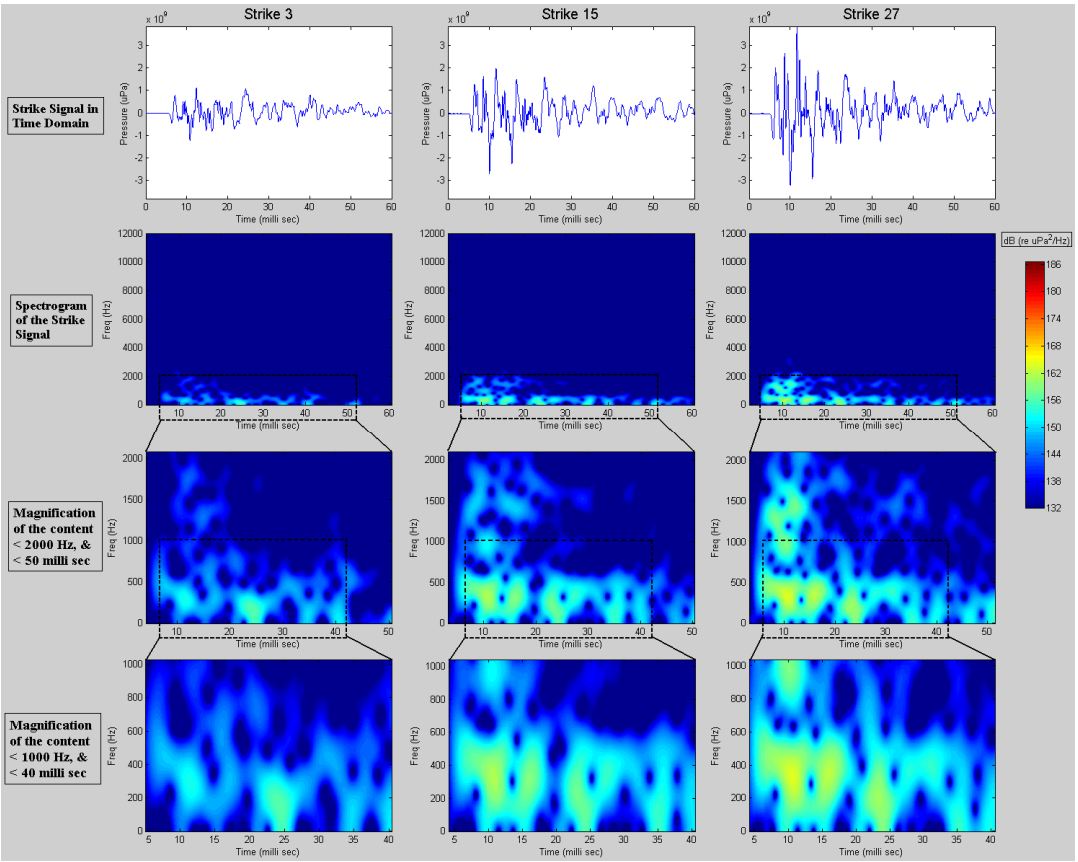

Figure 6.3 Time series and spectrograms of the TNAP protected pile R4 as the pile driving process progress

With the implementation of the TNAP, the "structure" of the residual noisy spots (the yellow spots in the spectrograms), which refer to the content whose magnitude exceed 165 dB (re 1μPa²/Hz), tends to be consistent from strike to strike. Figure 6.3 suggests these noisy spots appear most frequently at below 2000 Hz with the most energetic ones locate between 200 to 500 Hz.

In summery, the results in this chapter suggest the recurring locations of the noisiest spots of both pile T2 and R4 are mostly consistent across strike number. However, some spectral content variations are observed below 2000 Hz. For the unmitigated pile, T2, the noisiest spots consistently occur at below 2000 Hz with the loudest locate between 200 to 1000 Hz. After shrouding the driven pile with the TNAP, which is especially effective for mitigating noise above 2000 Hz, most of the residual noise locate below 600 Hz with the most energetic ones locate between 200 to 500 Hz.

7 Transmission Loss and Potential SEL Reduction

Prior to identifying the factors that are important in noise abatement, it is important to first understand the transmission loss across the attenuator. In this chapter, we first investigate the pile driving noise transmission decay across the TNAP and subsequently explore the areas where improvements can be made.

7.1 The transmission loss curve across the TNAP

In this study, transmission loss, or TL, is generated by finding the difference between the mean ESD curve of the bare pile, T2, and the mean ESD curve of the TNAP protected pile, R4. This estimate assumes that conditions for the two tests, e.g., hammer type, strike force, and measurement conditions, were the same when in fact these are not known. Nevertheless, it is of interest to evaluate the two cases, T2 and R4, from the standpoint of transmission loss to reach a better understanding of the physics of noise control. To estimate transmission loss the ESD data are examined as follows:

$$TL = 10\log_{10}(ESD_{pileT2}) - 10\log_{10}(ESD_{pileR4}) \quad \textbf{(7.1)}$$

The TL curve and the mean ESD curves are shown in Figure 7.1 and 7.2 below.

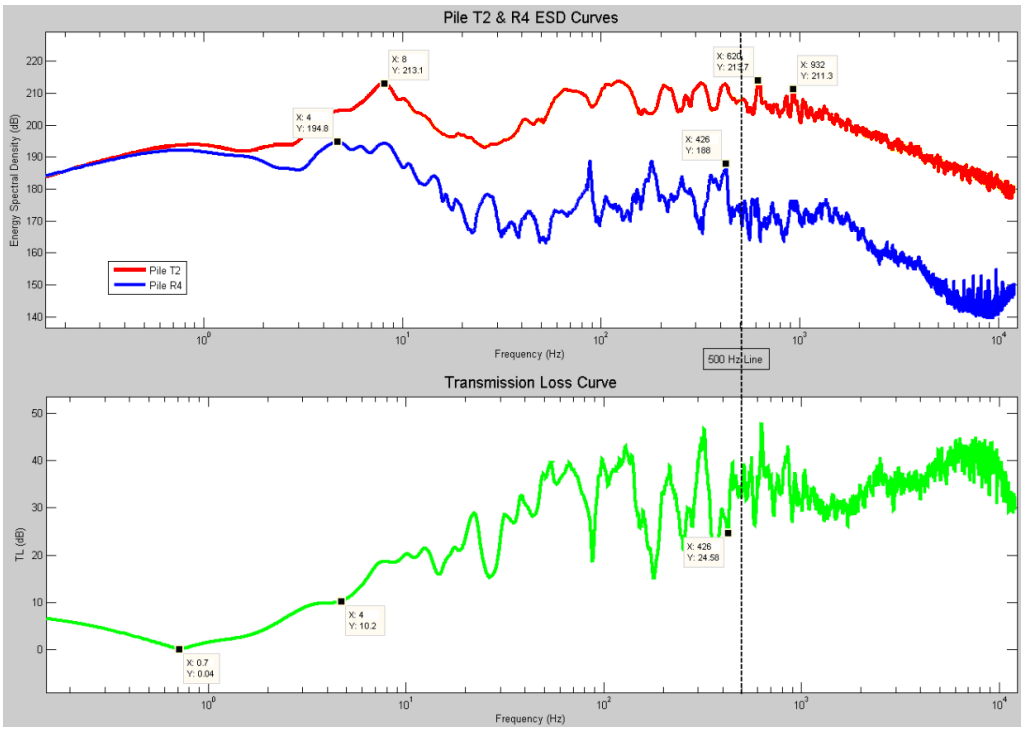

Figure 7.1 TL curve and mean ESD curves of pile T2 and pile R4 (< 12000Hz)

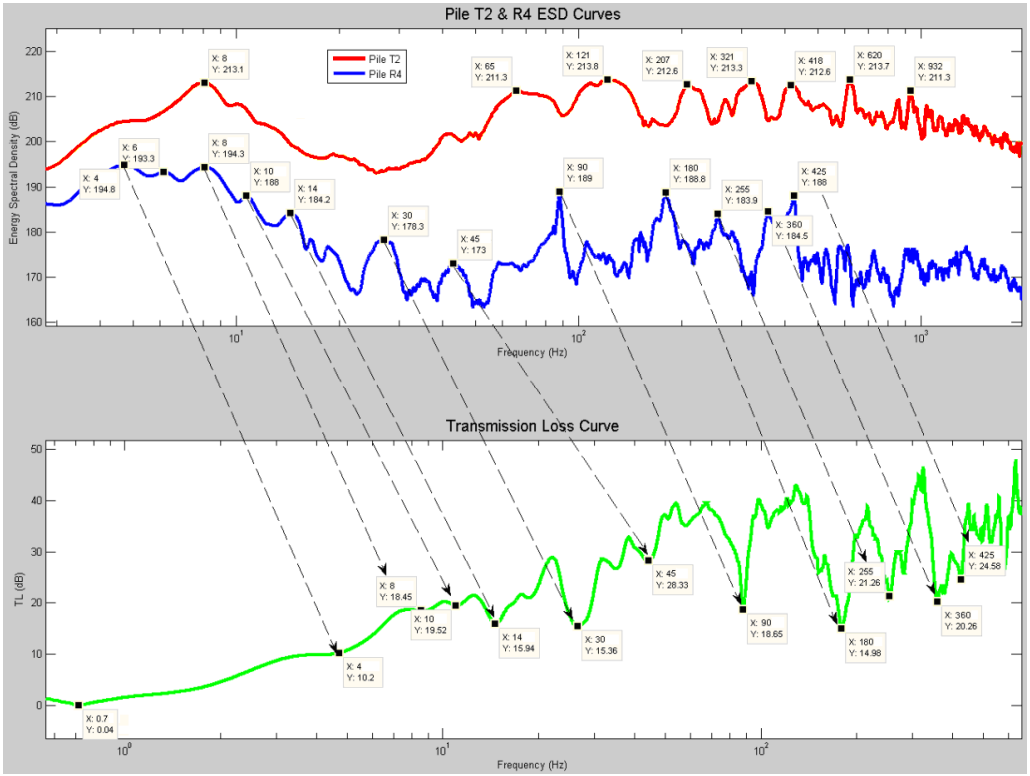

Figure 7.2 TL curve and mean ESD curves of pile T2 and pile R4 (< 500Hz)

According to the upper plot of Figure 7.1, the most energetic peaks of the TNAP protected pile R4 are below 500 Hz, and this will be the primary frequency range of interest as shown in Figure 7.2. Low transmission loss spots on the TL curve are primary targets of interest in regards to making the TNAP more soundproof. As the arrows in Figure 7.2 indicate, all of the low transmission loss spots are associated with the most energetic peaks of pile R4. Therefore, investigating the energy reduction associated with the elimination of these peaks would be essential for implementing cost-effective improvements, and such investigation will be conducted in the next section.

7.2 Potential SEL Reduction

The results in Chapter 2 indicate the cumulative SEL of the TNAP protected pile R4 exceeds the 183 dB_{SEL} interim criterion threshold limit for fish <2 g by 11 dB. Moreover, the study of the noise transmission loss characteristics across the TNAP in section 7.1 indicates further improvements can be made by reducing the energy of the remaining twelve major peaks of the TNAP protected pile R4. Since SEL is proportional to energy, in this section, we estimate the potential amount of SEL reduction that can be achieved by eliminating the remaining twelve peaks.

According to Chapter 2, the SEL of underwater acoustic events, which is the energy flux of the event, is calculated by summing the cumulative pressure squared and integrating over the time interval T as shown in Equation 7.2 below. The unit of SEL is in μPa²*Sec.

$$SEL = 10\log_{10}\{\int_0^T [P(t)]^2 dt\} \quad \textbf{(7.2)}$$

Where P(t) is the pressure of the acoustic event with unit in μPa; T is the time interval of the acoustic event, and it has unit in second. In conjunction with the Parseval's theorem shown in Equation 7.4, SEL can also be written as

$$SEL = 10\log_{10}(\sigma^2) \quad \textbf{(7.3)}$$

where σ^2 is the quantity proportional to the energy of the acoustic pressure, and it has dimension of uPa²*sec.

$$\int_0^T [P(t)]^2 dt = \sigma^2 = \int_0^{f_{max}} P(f)df \quad \textbf{(7.4)}$$

f_{max} is the Nyquist frequency. P(f), which has dimensions uPa²*sec/Hz, is the averaged and normalized 1-sided energy spectral density. The estimate P(f) is computed via the squared magnitude of the FFT of the raw pressure data that is expressed in uPa. P(f) is normalized such that its integral over the designated frequency range satisfies the condition of the Parseval's theorem shown in Equation 7.4. Afterward, cumulative integral operation is carried out as shown in Figure 7.3 to identify the relative contribution of the twelve major peaks to

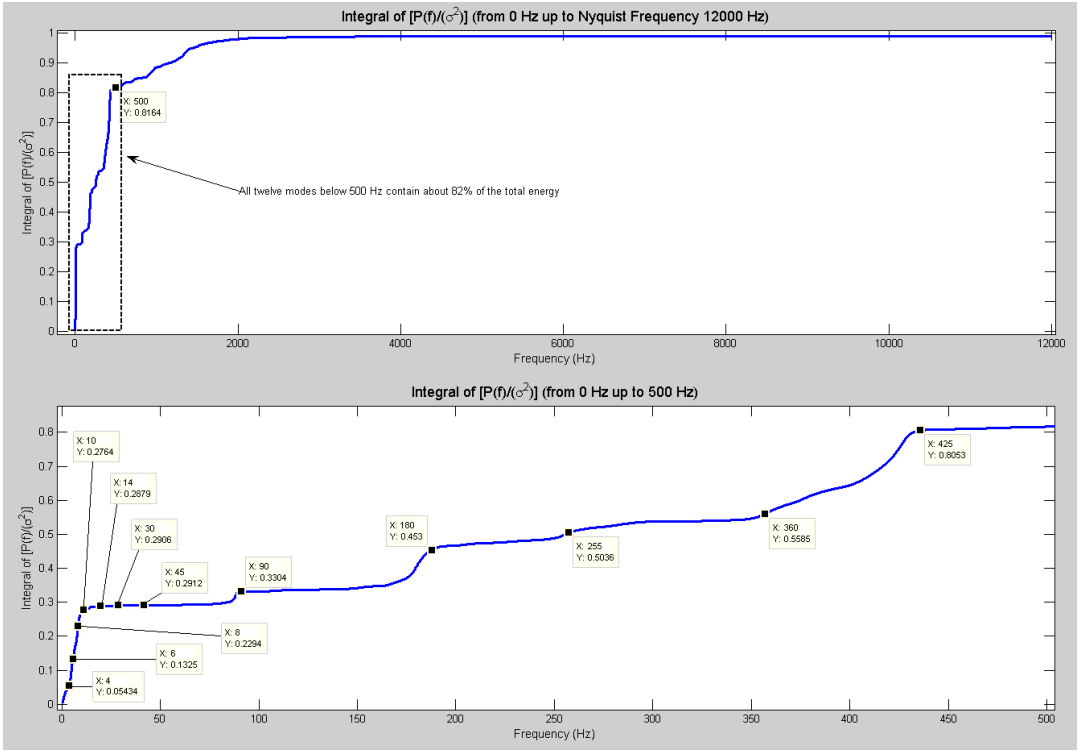

Figure 7.3 Energy contribution of the twelve peaks

the total energy of the ESD curve for pile R4. The integral is properly scaled by σ^2 hence it only reaches up to 1.0 (100%). A magnified view of the details below 500 Hz, where the twelve major peaks are, is illustrated in the lower plot. The twelve peaks are indicated by the black dots. A measure of the % energy contribution of each peak, η, is defined by subtracting the Y value of the previous peak from the Y value of the current peak. The ranking of this measure is listed in Table 7.1. According to the table, the twelve peaks contain about 82% of the total energy. In other words, approximately 7 dB_{SEL} reduction can be achieved if all twelve peaks were removed.

Table 7.1 Energy ranking of the twelve major peaks

Peak #	Peak Freq (Hz)	% Energy Contribution (η_{total} : 82 %) $\eta = Y_{current\ peak} - Y_{previous\ peak}$	Energy Ranking
1	4	5.4 %	6
2	6	8 %	4
3	8	10 %	3
4	10	5 %	8
5	14	1.2 %	10
6	30	0.3 %	11
7	45	0.06 % (Min)	12 (Lowest)
8	90	4 %	9
9	180	12 %	2
10	255	5.1 %	7
11	360	5.5 %	5
12	425	25 % (Max)	1 (Highest)

8 Natural Frequencies and Mode Shapes of the Partially Submerged Pipes

According to Chapter 5, the peak frequencies of pile T2 and the TNAP protected pile R4 are mostly consistent as a function of strike number. An interpretation that these peak frequencies are associated with structural resonances (i.e. as described in Chapter 3) is will be put forth in this chapter. Both pile T2 and the outer pipe of the TNAP are the most outer radiating component of the noise source since their vibration can transmit into the surrounding water effectively. The structural resonance modes of these two pipes may therefore be responsible for some of the underwater noise during pile driving. In this chapter, we identify the possible modal density and vibration mode shapes of the two pipes at their corresponding observed peak frequencies. In Chapter 4, we identify the possible vibration mode shapes associated with the most energetic natural frequencies of a pipe using a closed-form solution. However, there is no closed-form solution for the partially submerged pipe since the fluid loading only is not acting along the entire length of the pipe. Therefore, we use a finite element model (ANSYS) to explore the most energetic peaks of pile T2 and the TNAP protected pile R4. This thesis work has focused on the structural modes as being one source of the spectral peaks observed in energy spectra associated with underwater pile impact noise, the results of which will now be summarized in this chapter. It should be emphasized, however, that such peaks in the spectra may be the result of

reflections from nearby objects, such as the barge or other piles. Another source of these peaks may be due to the reflections of the longitudinal stress waves that is caused by the impact of the hammer. However, an exhaustive exploration of identifying the exact source of these peaks is beyond the scope of this work. Other mechanisms, less tied to structural resonant effects, are currently being investigated by our research group, and thus this particular work should be viewed as a useful first step in the comparison of various mechanisms for noise generation.

8.1 Identify when fluid loading is important

Since both pile T2 and the outer pipe of the TNAP are partially submerged, we need to first identify when fluid loading is important. The key difference between the dry section and the wetted section of a partially submerged pipe is that the later can be considered to have additional mass which consists of the mass of the internal fluid and the mass of the effective external fluid due to fluid loading. Assuming all internal and effective external fluid are completely lumped into the steel structure of the pipe and evenly distributed within the wetted section, the averaged density of the wetted section is defined in Equation 8.1 below. Where h is the pipe wall thickness, R is the mean radius, m_s is the mass per unit length of the structure, and m_i is the mass

per unit length of the internal water. ρ_{steel} = 7800 kg/(m^3) and ρ_{water} = 1030 kg/(m^3) are the density of steel and sea water, respectively.

$$\rho_{avg} = \frac{m_s + m_i + m_a}{\pi[(R+\frac{h}{2})^2 - (R-\frac{h}{2})^2]} \quad \textbf{(8.1)}$$

$$m_s = \pi\rho_{steel}[(R+\frac{h}{2})^2 - (R-\frac{h}{2})^2] \quad \textbf{(8.2)}$$

$$m_i = \pi\rho_{water}(R-\frac{h}{2})^2 \quad \textbf{(8.3)}$$

m_a is the added mass per unit length of the pipe due to fluid loading defined in Equation 8.4. As Figure 8.1 indicates, the axial mode number, *j*, of the pipe determines when fluid loading is important. Specifically, only when the bending wave number k_j of the pipe wall is greater than the acoustic wave number k in the external fluid, the added mass associated with fluid loading is significant [13]. Base on Figure 8.1, we can develop a methodology as shown in Figure 8.2 and 8.3 to identify which structural modes of pile T2 and the outer pipe of the TNAP are affected by fluid loading. For demonstration purpose, the maximum axial mode number, *j*, of the two provided examples in Figure 8.2 and 8.3 only reach up to 6. However, *j* practically can be any natural number.

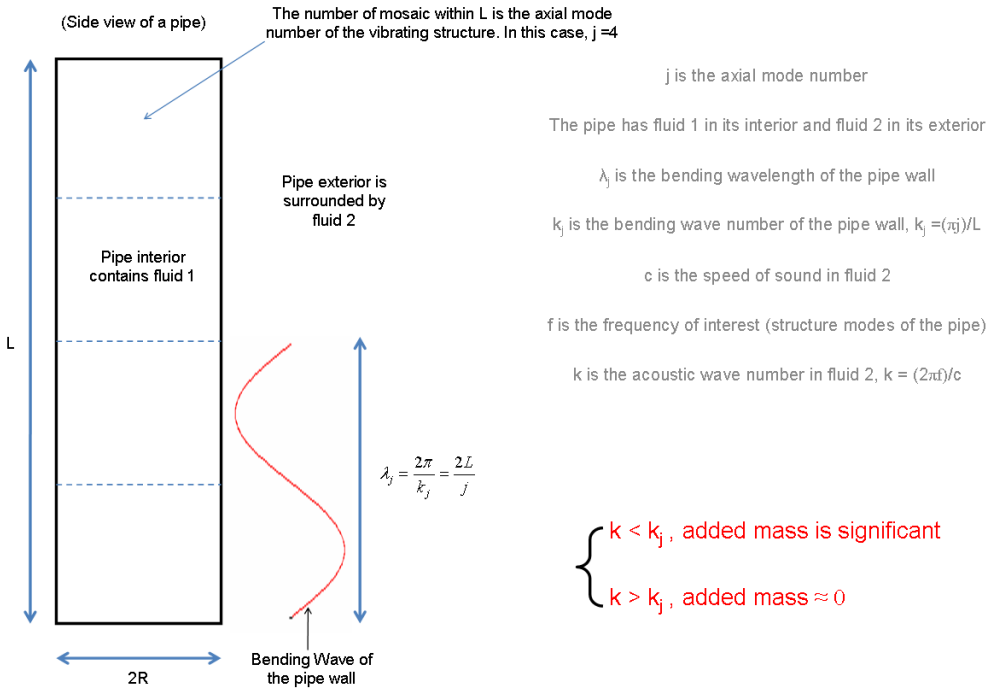

Figure 8.1 When fluid loading is important [13]

k_j is the bending wave number of the pipe wall, $k_j = (\pi j)/L$

k is the acoustic wave number in the pipe's external fluid, $k = (2\pi f)/c$

$k < k_j$, added mass is significant

$k > k_j$, added mass ≈ 0

Axial mode number j	1	2	3	4	5	6
k_j	0.1288	0.2577	0.3865	0.5154	0.6442	0.773

Compare k_j and k

The Pipe's Structure Resonance Freq (f) (listed in slide 7)	8	65	120	210	320	420	620	930
k	0.0341	0.2768	0.5093	0.8750	1.3442	1.7652	2.5975	3.9023

$k < \text{all } k_j$, so j=1~6 need added mass

$k < k_j$, when j≥3. so j=3~6 need added mass

$k < k_j$, when j≥4. so j=4~6 need added mass

$k > \text{all } k_j$, so j=1~6 added mass≈0

Figure 8.2 Identify which modes of pile T2 need to consider fluid loading

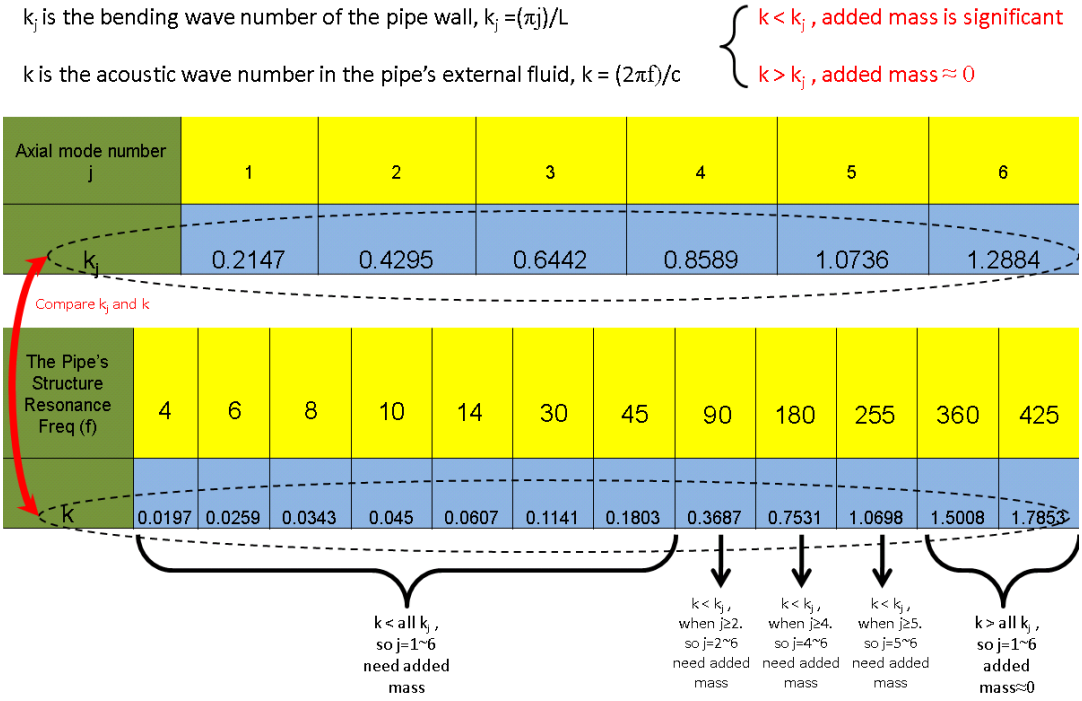

Figure 8.3 Identify which modes of the TNAP outer pipe need to consider fluid loading

8.2 Estimate the amount of added mass associated with fluid loading

After identifying when fluid loading is significant, the estimated amount of added mass per unit length m_a is defined by [10]:

$$m_a = \alpha[\rho_{water}\pi(R+\frac{h}{2})^2] \quad \textbf{(8.4)}$$

where α is the added mass coefficient which is determined by the aspect ratio L/(2R) of the pipe as shown in Table 8.1. L is the total length of the pipe, and R is the mean radius.

Table 8.1 Determine the added mass coefficient α

L/(2R)	1.2	2.5	5	9	∞
α	0.62	0.78	0.9	0.96	1

The data in Table 1.1 and 8.1 yield the added mass coefficients α of pile T2 and the outer pipe of the TNAP in Table 8.2.

Table 8.2 Added mass coefficient α of pile T2 and the TNAP outer pipe

Pipe of interest	Pile T2	TNAP outer pipe
L/(2R)	27.43	30.52
α	1	1

8.3 Boundary condition

Furthermore, according to the Mukilteo pile driving test report, the pile was driven in relatively soft sediments [4], which suggests the penetrated portion of the driven pile and the TNAP are expected to be able to deform freely in the soil. We employ a pinned boundary condition at the bottom of the driven pile and the outer pipe of the TNAP in the simulation to prevent the pipe from expanding radially at the bottom. The hammer strike on the pipe was approximated by an impulse excitation at the top of the structure.

8.4 Simulation results

The analysis flow chart in Figure 8.4 summarizes the setup of the simulation from section 8.1 through 8.3.

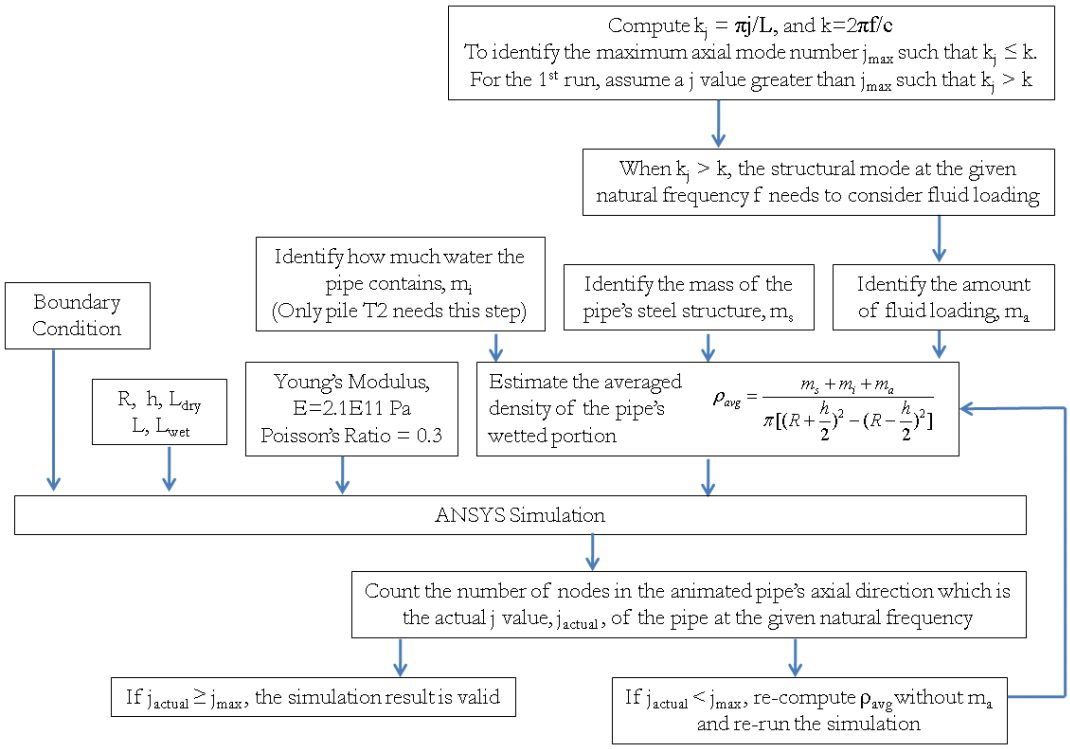

Figure 8.4 ANSYS simulation setup flow chart

The simulation results of pile T2 are shown in Figure 8.5 through 8.9. Figure 8.5 and Table 8.3 illustrate the possible modal density within the ±5 % frequency band of the observed peak frequencies. All possible structural modes of pile T2 which lie within the ±5 Hz frequency band of the observed peak frequencies are presented in Figure 8.7 through 8.9.

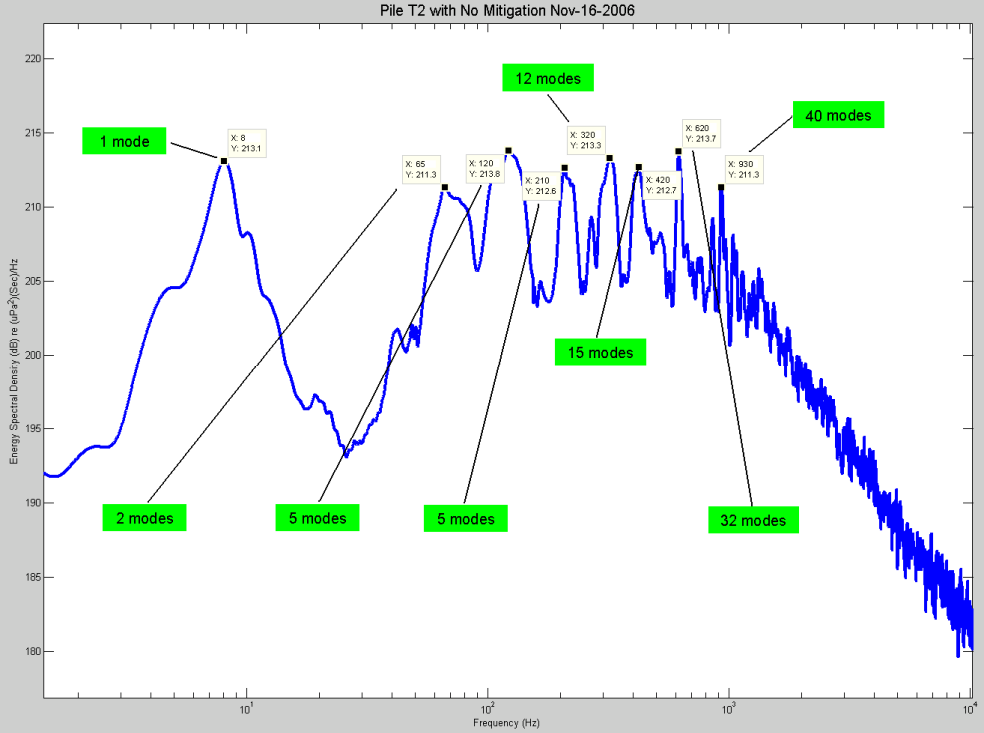

Figure 8.5 Possible modal density at the observed peak frequencies of pile T2 (±5% with respect to the observed peak frequencies)

Table 8.3 Modal density of the observed peaks for pile T2

Peak Freq (Hz)	65	120	210	320	420	620	930
Band Width (±5 % with respect to peak freq)	62~68	114~126	200~220	304~336	400~441	589~651	883~976
Number of modes	2	5	5	12	15	32	40
Modal density, (number of modes/band width)	0.33	0.43	0.25	0.38	0.37	0.52	0.42

Unlike the results of the pipe striking experiment in Chapter 4 which indicate all of the most energetic natural frequencies are associated with the shell modes (i=2~4) of the excited pipe, the results in Figure 8.6 suggest the lowest peak of

pile T2 may be caused by beam modes (i=1), whereas the upper seven peaks (between 60 to 1000 Hz) may be caused by the combination of breathing modes (i=0) and shell modes (i=2~5).

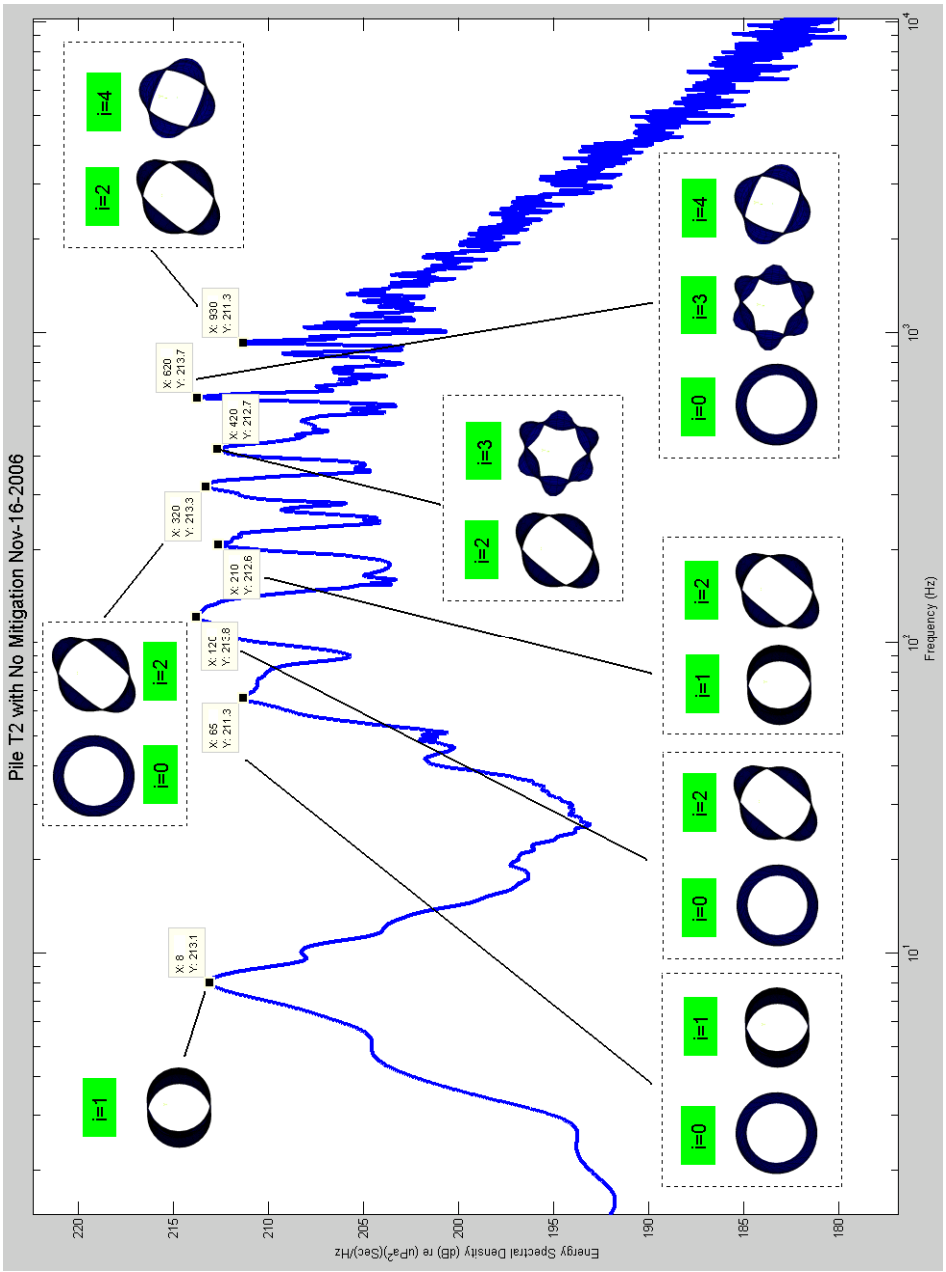

Figure 8.6 Possible circumferential mode shapes at the observed peak frequencies of pile T2

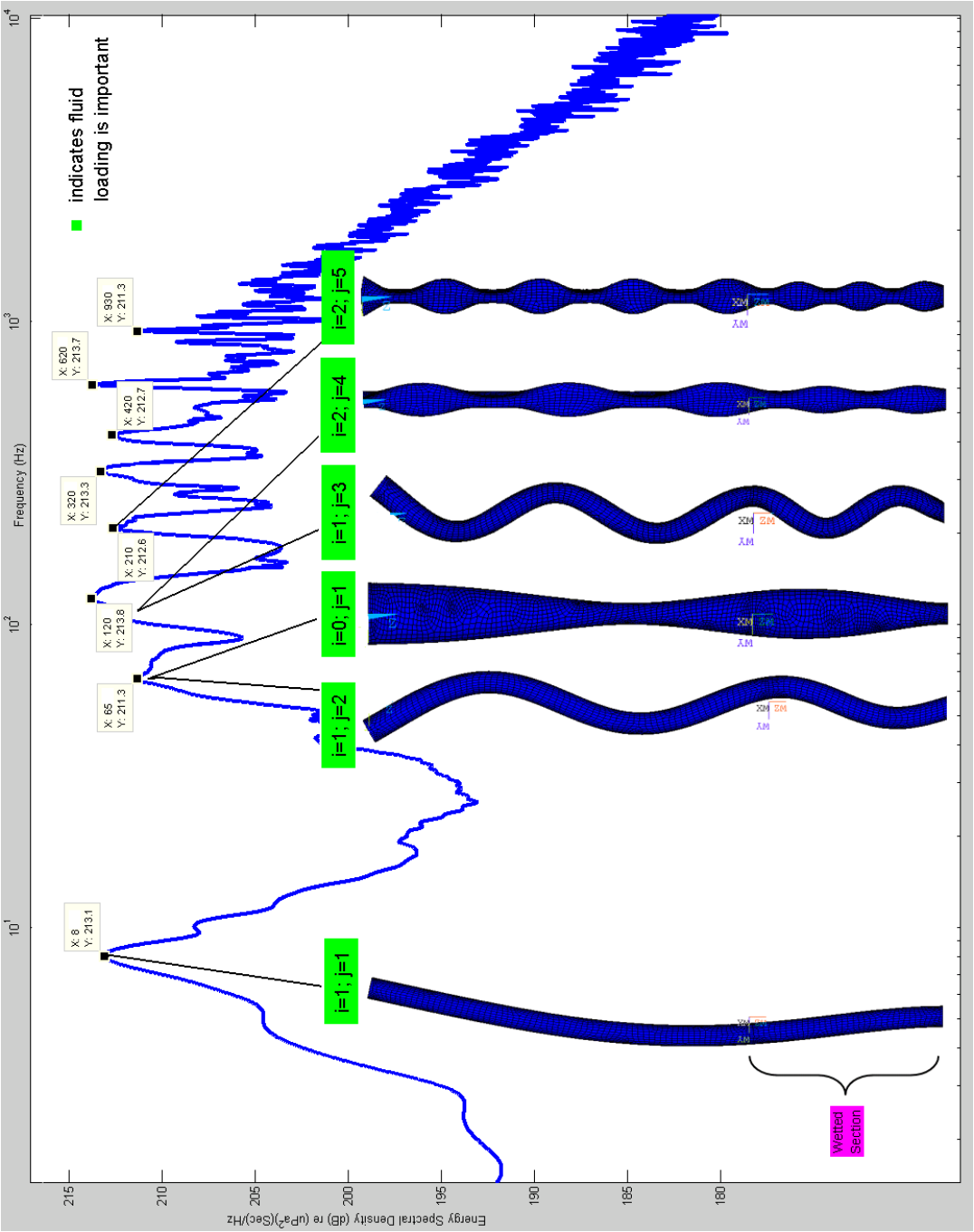

Figure 8.7 Possible axial mode shapes at the observed peak frequencies (≤ 210 Hz) of pile T2

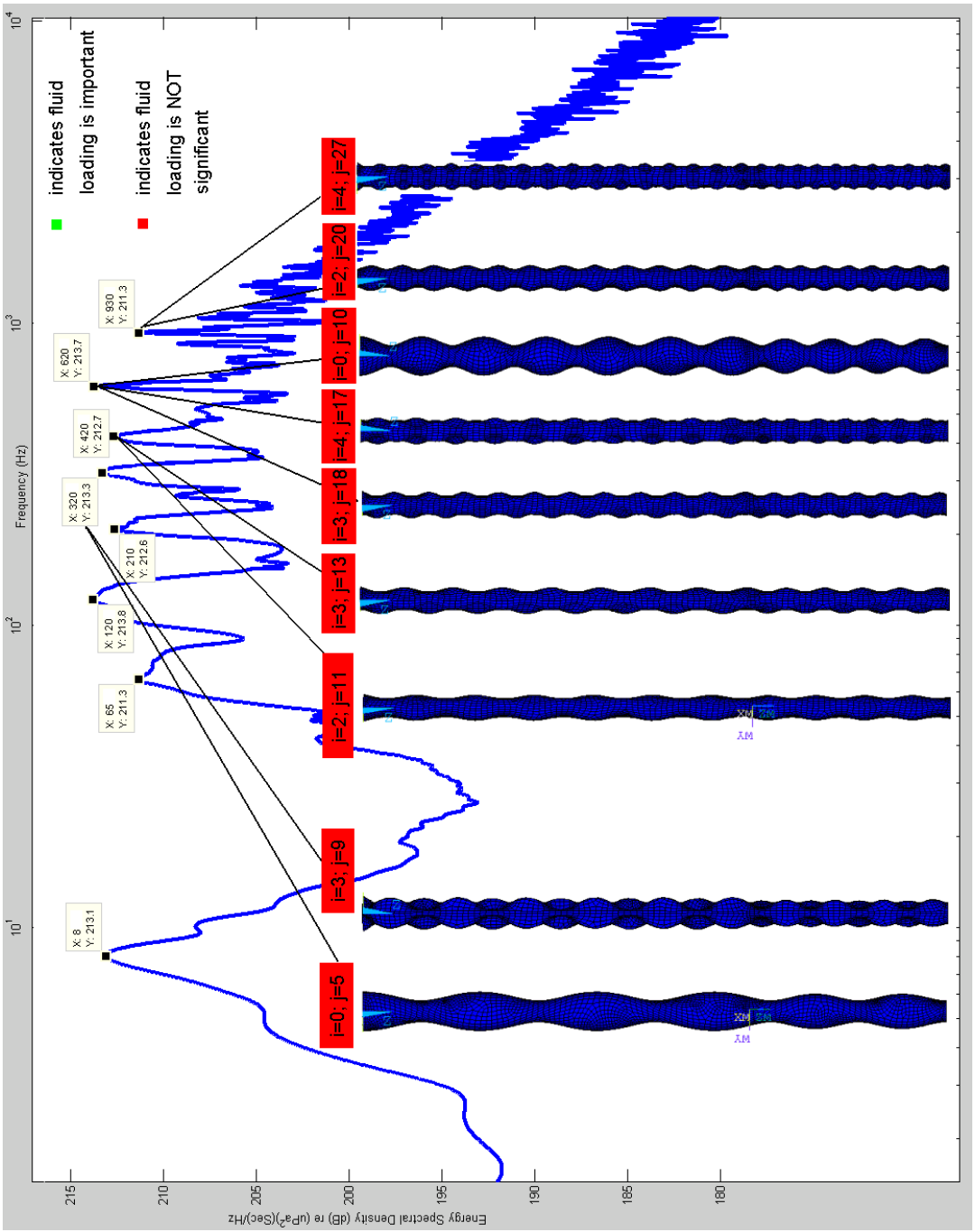

Figure 8.8 Possible axial mode shapes at the observed peak frequencies (> 210 Hz) of pile T2

Similarly, the simulation results of the TNAP outer pipe are shown in Figure 8.9 through 8.12. The possible modal density of the outer pipe at the observed peak frequencies are shown in Figure 8.9 and Table 8.4.

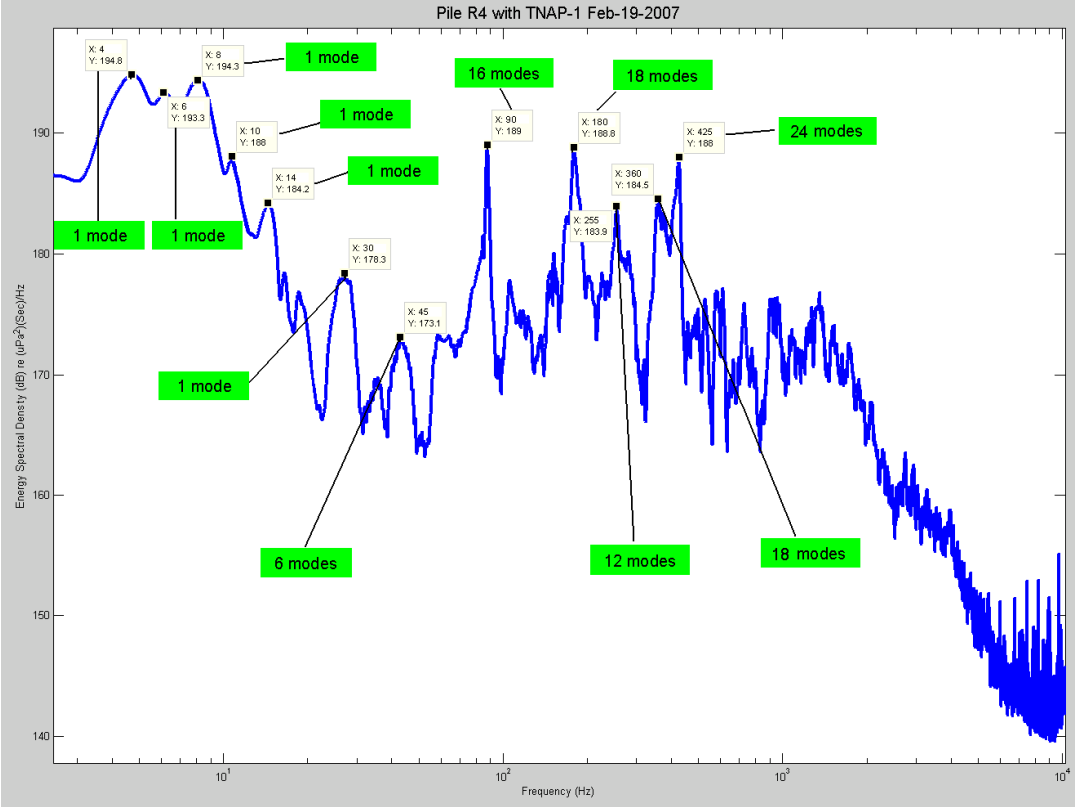

Figure 8.9 Possible modal density of the outer pipe at the observed peak frequencies of pile R4 (±5% with respect to the observed peak frequencies)

Table 8.4 Modal density of the TNAP outer pipe

Peak Freq (Hz)	45	90	180	255	360	425
Band Width (±5 % with respect to peak freq)	42~47	85~94	171~ 189	242~ 267	342~ 378	403~ 446
Number of modes	6	16	18	12	18	24
Modal density, (number of modes/band width)	1.2	1.78	1	0.48	0.5	0.56

All possible structural modes of the outer pipe which lie within the ±5 Hz frequency band of the observed peak frequencies are presented in Figure 8.10 through 8.12. The results in Figure 8.10 indicate that the three lowest peak

frequencies (<10 Hz) of the TNAP protected pile R4 are likely beam modes of the outer pipe, whereas the three peaks between 10 and 20 Hz may be caused by breathing modes (i=0), and the upper seven peaks (from 30 to 500 Hz) are shell modes (i=2~7) of the outer pipe.

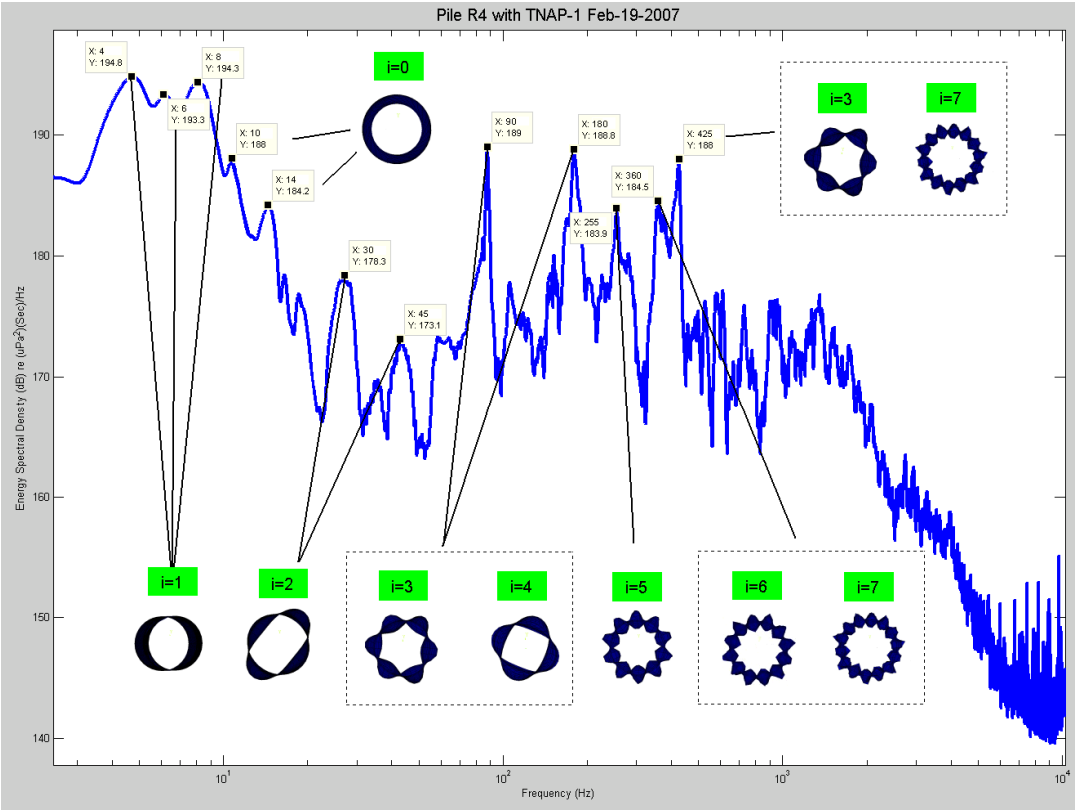

Figure 8.10 Possible circumferential mode shapes of the TNAP outer pipe at the observed peak frequencies of pile R4

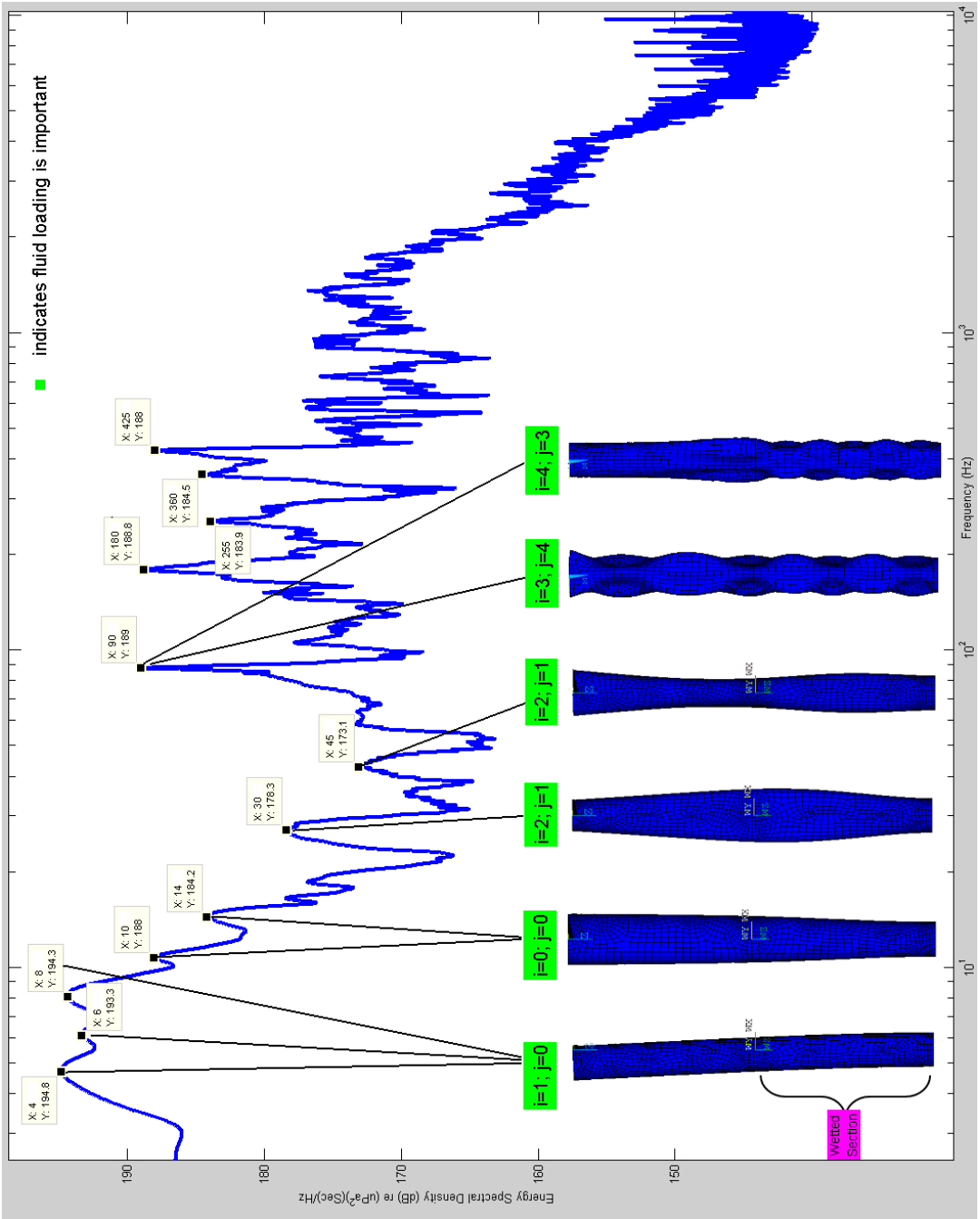

Figure 8.11 Possible axial mode shapes of the TNAP outer pipe at the observed peak frequencies (≤ 90 Hz) of pile R4

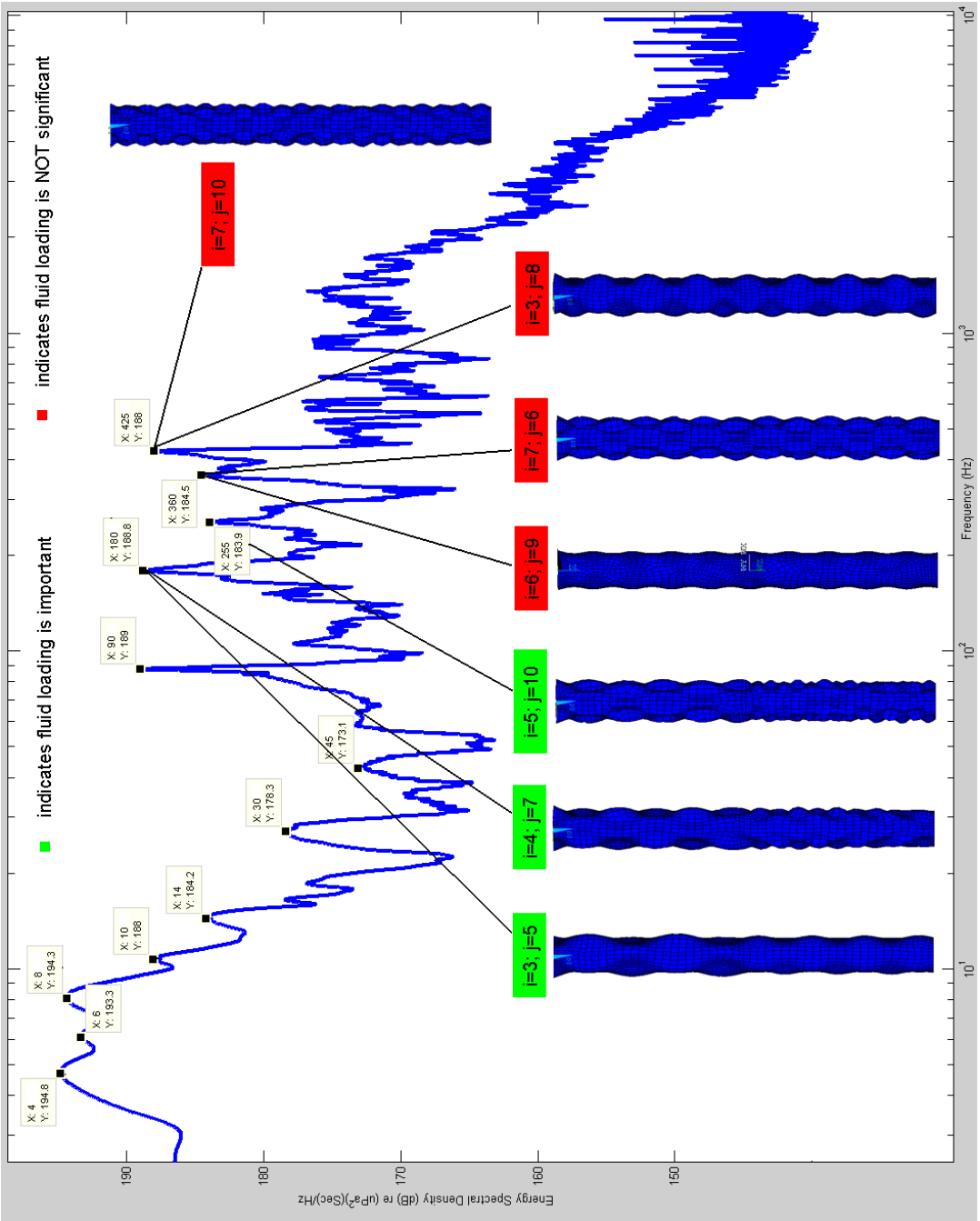

Figure 8.12 Possible axial mode shapes of the TNAP outer pipe at the observed peak frequencies (> 90 Hz) of pile R4

9 Conclusion

Noise test data from a bare pile, T2, and a double-walled TNAP protected pile, R4, from WSDOT's 2006 and 2007 Mukilteo Ferry Terminal pile driving project are analyzed in this study. It helps us to better understand underwater noise associated with the driven pile and the performance of the double-walled TNAP noise attenuation measure. The two pile driving tests were conducted with four months apart, and their direct comparison is complicated by this fact. Thus, although their comparison is carried out in this work, strictly speaking this thesis represents a two separated systems. The noise level of the two piles with respect to the 2008 interim criteria for injuring fish from pile driving (set by Fisheries Hydroacoustic Working Group [3]) are investigated in Chapter 2. Dual criteria (L_{peak} and cumulative SEL) are used by the regulatory bodies in June 2008 to provide protection to fish by limiting L_{peak} of a single hammer blow to 206 dB_{peak}, and the cumulative SEL of successive hammer strikes within a finite time window to 187 dB_{SEL} for fish ≥2 g and 183 dB_{SEL} for fish <2 g. The results indicate the cumulative SEL of both pile T2 and the TNAP protected pile R4 exceed both 187 dB_{SEL} and 183 dB_{SEL} interim criteria. Specifically, the noise level of pile T2 and pile R4 exceed the 183 dB_{SEL} interim criterion by 28 dB and 11 dB, respectively. Whereas 52% of the strikes on pile T2 breach the 206 dB_{peak} threshold limit. On the other hand, all L_{peak} values of the TNAP protected pile R4 comply with the 206 dB_{peak} criterion, but

they are still high enough to exceed the limit that has been set for foraging marbled murrelets; whereas the RMS values of pile R4 are also sufficiently high to exceed the limits established for the disturbance of cetaceans, pinnipeds and fish.

Chapter 3 and 4 are devoted to investigate which structural modes are more likely to be significantly excited when the pipe is subjected to excitation from hammer strikes. An experiment with a small pipe was conducted to shed light on this issue. The experiment showed that the lower modes of the pipe (480 – 13200 Hz) were significantly excited by the hammer strikes. The addition of damping material to the pipe was shown to reduce the acoustic energy of modes greater than 2500 Hz. On the other hand, the modes below 2500 Hz are likely shell modes of the pipe with low circumferential mode (i=2~4) and low axial mode numbers (j=1~4).

Time-frequency analysis on both pile T2 and pile R4 were presented in Chapter 6. After the TNAP is implemented, the results suggest most of the residual noise locates between 200 to 500 Hz. The recurring locations of the noisiest spots in time-frequency space of both piles are mostly consistent as the piles being driven further into the ground. However, some spectral content variations are observed below 2000 Hz. Hence, an investigation regards to these

variations is conducted in Chapter 5. The results suggest the mean ESD curves of both pile T2 and pile R4 represent the rest of the data across frequency spectrum from about 3 Hz up to Nyquist frequency 12000 Hz. Since the variations are small, the mean peak ESD values and mean peak frequency values of both piles are consistent as a function of strike number.

The transmission loss across the TNAP is analyzed in Chapter 7. The results indicate the TNAP can effectively attenuate noise >1000Hz, and the most energetic residual noise is associated with the twelve lowest peaks of the TNAP protected pile R4. All these peaks are below 500 Hz. An investigation on cumulative SEL reduction associated with the elimination of these twelve peaks was performed. The results suggest that all twelve peaks contain about 82% of the total energy. An approximately 7 dB_{SEL} reduction can be achieved if all twelve peaks were eliminated.

Finally, we used finite element modeling in Chapter 8 to investigate the modal density and the possible mode shapes of the partially fluid loaded pile T2 and the outer pipe of the TNAP at their corresponding observed peak frequencies. Unlike the results of the pipe striking experiment which indicated that only shell modes (i=2~4) were excited by the hammer strikes, the results of pile T2 suggest the lowest peak frequencies (<10 Hz) may be caused by beam

modes (i=1), whereas the upper seven peak frequencies (between 60 to 1000 Hz) may be caused by the combination of breathing modes (i=0) and shell modes (i=2~5). Similarly, the results of the TNAP outer pipe indicate that the three lowest peak frequencies (<10 Hz) are likely beam modes, whereas the three peaks between 10 and 20 Hz may be caused by breathing modes (i=0), and the upper seven peaks (from 30 to 500 Hz) are shell modes (i=2~7) of the outer pipe.

This thesis work has focused on the structural modes as being one source of the spectral peaks observed in energy spectra associated with underwater pile impact noise. It should be emphasized, however, that such peaks in the spectra may be the result of reflections from nearby objects. Another source of these peaks may be due to the reflections of the longitudinal stress waves that is caused by the impact of the hammer. Other mechanisms, less tied to structural resonant effects, are currently being investigated by our research group, and thus this particular work should be viewed as a useful first step in the comparison of various mechanisms for noise generation.

10 Reference

1. K.-H. Elmer, W.-J. Gerasch, Inst. für Statik und Dynamik, Leibniz Universität Hannover (ISD), T. Neumann, J. Gabriel, DEWI, K. Betke, M. Schultz-von Glahn, Inst. für technische und angewandte Physik, Oldenburg (itap), "Measurement and Reduction of Offshore Wind Turbine Construction Noise." DEWI Magazine, February 2007. 33-38

2. Arthur Popper, Thomas Carlson, Anthony Hawkins, Brandon Southall, Roger Gentry, "Interim Criteria for Injury of Fish Exposed to Pile Driving Operations: A White Paper", 2006

3. "Agreement in Principle for Interim Criteria for Injury to Fish from Pile Driving Activities", June 12th, 2008

4. Jim Laughlin, "Underwater Sound Levels Associated with Driving Steel and Concrete Piles Near the Mukilteo Ferry Terminal", WSDOT report, March, 2007

5. Regulatory bodies [3] include U.S. Federal Highway Administration, NOAA Fisheries Northwest and Southwest Regions, U.S. Fish and Wildlife Service

Regions 1 & 8, California/Washington/Oregon State Departments of Transportation, California Department of Fish and Game.

6. Washington State Department of Transportation, Noise Assessment Guidance, Projects with Pile Driving, Marine Mammal, Fish, and Marbled Murrelet Injury and Disturbance Thresholds for Marine Construction Activity. WSDOT report, April, 2009

7. Jim Laughlin. "Underwater Sound Levels Associated with 'Dry' pile driving at the Evans Creek Bridge on SR 202", WSDOT report, September. 2006

8. Washington State Department of Transportation. Interim Criteria for Injury of Fish Exposed to Pile Driving Operations: A White Paper, p10, May. 2006

9. Kaiser windowing function is one-parameter family of window functions used for digital signal processing. Kaiser function provides good amplitude accuracy, low spectral leakage and fair frequency resolution. kaiser (150, 5) returns a 150 point Kaiser window. The 2nd number affects the side lobe attenuation of the Fourier transform of the window. Increasing it widens the main lobe and decreases the amplitude of the side lobes. By choosing such number to be ≥4.5 in MATLAB, the side lobes are sufficiently suppressed (≥ -

70 dB with respect to the main lobe) to prevent the spectral leakage from causing misleading information about the spectral amplitude and frequency.

10. Blevins, Robert, "Formulas for Natural Frequency and Mode Shape", 291-317 (1984 Edition)

11. Sharama, C. B. "Simple Linear Formula for Critical Frequencies for Cantilevered Circular Cylindrical Shells," J. Sound Vib. 55, 467-471 (1977)

12. Cyril M. Harris. "Shock Vibration Handbook", 7-36 (3rd Edition)

13. William Blake. "Mechanics of Flow-Induced Sound and Vibration", 328-338 (1986)